

Effect of aspect ratio on the unlimited flow-induced vibration of an elliptical cylinder-plate assembly

Ying Wu ^{1,*} Fue-Sang Lien ¹ Eugene Yee ¹ and Guang Chen²

¹*Mechanical and Mechatronics Engineering Department, University of Waterloo,
200 University Avenue West, Waterloo, N2L 3G1, Ontario, Canada*

²*School of Traffic and Transportation Engineering, Central South University, No. 22 Shaoshan South Road,
Tianxin District, Changsha, 410075, Hunan, China*



(Received 27 June 2023; accepted 14 March 2024; published 6 May 2024)

The transverse flow-induced vibration (FIV) of an elastically supported elliptical cylinder-plate assembly is investigated numerically for a laminar flow at a Reynolds number of 100. The aspect ratio (AR) of the elliptical cylinder is varied over a range of values (namely, $AR = 0.5, 0.67, 0.75, 1, 1.5,$ and 2). In addition, two normalized splitter-plate lengths, $L_{SP}/D = 0.75$ and 2.5 , are investigated (where L_{SP} is the splitter-plate length, and D is the equivalent diameter of the elliptical cylinder). A low mass ratio of 10 and zero structural damping are used in the numerical simulations to induce larger oscillations in the assembly. The numerical results show that all cases investigated exhibit a FIV over an unlimited range of reduced velocity. An increase in the AR promotes the vibrations of the assembly through a reduction in the reduced velocity associated with the onset of FIV and a concomitant increase in the vibration amplitude. In addition, a larger AR facilitates the transition from a pure galloping (for $AR \leq 1$) to an integrated VIV-galloping response (for $AR > 1$) for an assembly with $L_{SP}/D = 0.75$. Moreover, a larger AR significantly decreases the onset velocity of galloping for an assembly with $L_{SP}/D = 2.5$. The AR determines the nature and width of the synchronization branch in the amplitude response. In general, a larger AR leads to the inception of higher-order synchronization branches in the amplitude response and to the suppression of some branches (e.g., still and initial galloping branches) for assemblies with long splitter plates. Finally, with respect to the flow dynamics associated with an unlimited FIV, increasing AR promotes the shedding of more complex vortices in the wake of the assembly (e.g., the emergence of a tail-shaped vortex and a slender vortex)—despite this, the wake mode remains unaltered.

DOI: [10.1103/PhysRevFluids.9.054102](https://doi.org/10.1103/PhysRevFluids.9.054102)

I. INTRODUCTION

The two-way fluid-structure interaction (FSI) problem of flow-induced vibration (FIV) of a bluff body has received a great deal of attention. Indeed, FIV can be either desirable or undesirable depending on the engineering structure it affects (e.g., marine risers, cables, bridges, energy harvesters). Moreover, FIV has a huge amount of potential for fluid (e.g., wind, water) energy harvesting, such as the vortex-induced vibration aquatic clean energy (VIVACE) harvester proposed by Bernitsas *et al.* [1]. Vortex-induced vibration (VIV) and galloping are the two most extreme types of FIV—the first is a forced resonance caused by alternating vortex shedding and is characterized by a large-amplitude vibration that occurs within a narrow range of velocity (i.e., lock-in), while the second is a self-excited instability that occurs over an unlimited range of velocity [2]. Due to

*y753wu@uwaterloo.ca

its wider effective velocity range (with structural oscillation) and greater vibration amplitude, the galloping-dominated response often outperforms VIV in the context of energy harvesting based on the oscillatory motions.

An appropriate configuration of the flow incidence angle [3,4], the mass-damping parameter [5,6], and the Reynolds number [7] can cause a square cylinder to gallop—this is a classic example used in the investigation of an unlimited FIV response. In this case, when the reduced velocity exceeds a critical value required for the onset of FIV, the oscillatory response exhibits a monotonically increasing amplitude with increasing reduced velocity [4]. It should be noted that an unlimited FIV response can also be generated on an isolated cylinder with various noncircular (e.g., rectangular, triangular, or elliptical) cross-sections or on a passive turbulence control (PTC) cylinder (e.g., a cylinder-plate assembly). The geometrical shape of the structure essentially determines its dynamic response.

A number of experimental and numerical studies has investigated how the cross-sectional side ratio defined as $SR = b/d$ (where b and d are the side lengths of the body in the transverse and streamwise flow directions, respectively) affects the FIV response of a rectangular prism (viz., generalization of a square cylinder) [8–10]. In a numerical study, Zhang *et al.* [8] revealed that a high SR had a positive impact on the FIV of an elastically mounted rectangular cylinder, with $SR = 0.5$ – 6.0 in the Reynolds number range of 7500 – $187\,500$. More specifically, for the smallest value of $SR = 0.5$ investigated, no VIV or galloping was reported. However, for $SR = 0.67$, an unlimited galloping with a large onset velocity was observed. Moreover, for $SR = 0.83$ – 4 , an unlimited FIV associated with a one-third lower onset velocity occurred, which was a strong interference between VIV and galloping. The oscillations for $SR = 0.67$ – 4 displayed an increasing vibration amplitude with velocity. For $SR = 6$, the FIV still occurred over an unlimited velocity range, but the vibration amplitude remained unchanged after the galloping onset. Zhao *et al.* [9] conducted experimental tests on a variety of rectangular cylinders with $SR = 2$ – 5 for a Reynolds number between 940 and 8200 . In contrast with the previous examples which exhibited an integrated VIV-galloping regime with an unconstrained amplitude response as a function of the reduced velocity, a maximum SR of 5 was associated with a limited FIV response. Moreover, it was reported that a change in SR from 2 to 4 led to an increase in the local peak amplitude. In accordance with these two studies, a rectangular prism with a SR of roughly 0.67 – 4 is most likely to provoke an unlimited FIV response—within this range, a greater SR will induce an unlimited FIV through an increase in the vibration amplitude and a decrease in the onset velocity.

An elliptical cylinder, a triangular prism, and a trapezoidal cylinder are also susceptible to an unlimited FIV response. A number of investigations involving an elastically mounted elliptical cylinder [11,12] have demonstrated that a larger aspect ratio $AR = b/a$ (where b and a are the lengths of the ellipsoidal cylinder in the transverse and streamwise flow directions, respectively) provokes a larger vibration amplitude and a wider reduced-velocity range for the FIV of the structure. Moreover, the rotary motion of an elliptical cylinder can promote its translational oscillation. According to Zhu *et al.* [13], the transition from a restricted VIV to an unlimited galloping occurred in a freely rotatable elliptical cylinder with $b/a = 0.5$ and with a moderate torsional friction. The transverse vibration of a low-AR elliptical cylinder with $b/a = 0.5$ – 1 was also amplified by the addition of a rotating degree of freedom (DOF) [14,15]. For an isosceles triangular prism, the AR is a three-dimensional concept, viz., $AR = H/D$, where H and D are the prism height and prism projection width, respectively. The influence of AR of a triangular prism on its FIV was studied by Shao *et al.* [16]. These investigators reported that, whereas an unrestricted VIV-galloping response was induced in the triangular prism with $H/D = 1$ and 1.5 , only a limited VIV was provoked in the prism with $H/D = 0.5$ and 0.85 . The vibration amplitude of an unlimited FIV was, however, reduced with an increase in the prism AR. Both square and triangular cylinders can be considered specific examples of a trapezoidal cylinder characterized by the $AR = d/D$ (where d and D are the lengths of the shorter and longer sides of a trapezoidal cylinder). In the experimental investigations by Zhu *et al.* [17], an unlimited galloping response was reported for a trapezoidal cylinder with

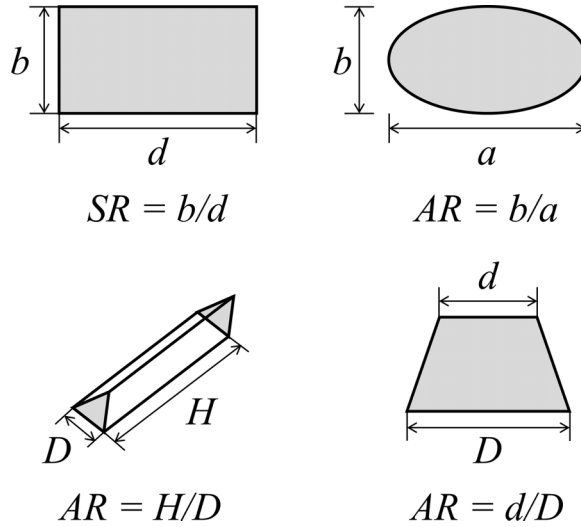


FIG. 1. Definition of the aspect ratio for various cross-sectional body shapes.

$d/D = 0.3, 0.5,$ and 0.7 . Figure 1 compares the definition of the AR for different cross-sectional body shapes.

A cylinder with a splitter-plate attachment can also experience an unlimited FIV response. Most investigations of a cylinder-plate assembly focus on the effect of plate length on the dynamic response of the assembly or report the types of oscillations that can occur in this structure (e.g., VIV, galloping, integrated or separated VIV and galloping) [18–22]. Wu *et al.* [23] conducted a series of numerical simulations to study the free vibrations of an elliptical cylinder with a fixed-length splitter plate ($L_{SP}/D = 0.5$) and investigated the influence of $AR = 0.5$ – 2 on the FIV of the assembly. These investigators reported that a larger AR led generally to an increase in the resulting vibration amplitude in the assembly, but the effective reduced-velocity range for the largest AR investigated in this paper (viz., $AR = 2$) was paradoxically narrower.

The review above shows that, in addition to changing the strength of the structural oscillation and triggering the transition between the different FIV modes, the AR of a cylinder can have a significant influence on many other aspects of the FIV response of an elliptical cylinder-plate assembly. Nevertheless, to date, little research has been conducted on the impact of AR on the dynamic response of this PTC cylinder. To this purpose, Wu *et al.* [23] conducted some seminal work on the FIV response over a restricted reduced-velocity range of an elastically mounted elliptical cylinder-plate assembly with ARs in the span $0.5 \leq AR \leq 2$ and a fixed splitter-plate length $L_{SP}/D = 0.5$. However, their investigation was restricted only to oscillations that occur over a limited range of reduced velocity (viz., to self-limited FIV). In such a context, the objective of this paper involves the extension (generalization) of this previous effort to study the synergy effect of the $AR = 0.5$ – 2 and the splitter-plate length ($L_{SP}/D = 0.75$ and 2.5) on the FIV of an elliptical cylinder-plate assembly and, more particularly, to investigate the dynamics of an unlimited FIV response of this assembly over a wide reduced-velocity range.

This paper is organized as follows. Numerical modeling of the two-way FSI of an elastically mounted elliptical cylinder-plate assembly is described in Sec. II. The numerical results of the unlimited FIV response of the assembly and its dynamical characteristics are presented and discussed in Sec. III. The key takeaways and main conclusions are summarized in Sec. IV.

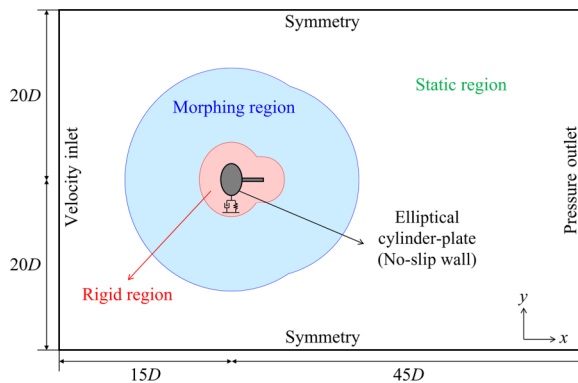


FIG. 2. An elastically mounted elliptical cylinder-plate assembly. The computational domain is partitioned into three regions, and the boundary conditions imposed in our numerical simulations are exhibited. The assembly is supported on a mass-spring-damper system that is constrained to oscillate only in the transverse (or y) direction.

II. NUMERICAL METHODOLOGY

As shown in Fig. 2, an elliptical cylinder-plate assembly is elastically supported by a mass-spring-damper system and is constrained to oscillate only in the transverse (or y) direction to give a single-DOF (SDOF) dynamical system. The incident velocity is along the streamwise (x) direction with a constant value of U . It should be stressed that, in this paper, we focus on the low-Reynolds number FIV of a SDOF system without any rotation. The reason for this is twofold: (1) the transverse DOF is associated with the dominant dynamic effects of the assembly—in comparison, the streamwise and/or rotational DOF in the assembly correspond to secondary (weaker) effects, and (2) the limited computational resources only allow for a large number of simulations required in this paper to be conducted for a low-Reynolds number laminar flow.

A number of numerical simulations are conducted of the flow past the elastically mounted elliptical cylinder-plate assembly for $AR = 0.5, 0.67, 0.75, 1, 1.5,$ and 2 and for $L_{SP}/D = 0.75$ and 2.5 —the splitter-plate width is fixed at $W_{SP}/D = 0.06$. As shown in Fig. 1, the AR of an elliptical cylinder is $AR \equiv b/a$. Following Wu *et al.* [23], D used in the normalization of the splitter-plate size is defined as the diameter of the equivalent circular cylinder whose cross-sectional area is equal to that of the elliptical cylinder [viz., $D = 2(ab)^{1/2}$], which has a fixed value of $D = 1$ m in our numerical simulations. The two splitter-plate lengths of $L_{SP}/D = 0.75$ and 2.5 are specifically chosen because a circular cylinder-plate assembly with these lengths are associated with an integrated VIV-galloping and a separated VIV and galloping response, respectively [22,24]. Furthermore, these oscillations correspond to unlimited FIV responses, with the vibration amplitude increasing monotonically with the reduced velocity U_r .

The computational domain and the boundary conditions applied in the numerical simulation are also shown in Fig. 2. The domain size ($60D \times 40D$) is chosen based on a comprehensive sensitivity analysis conducted by Wu *et al.* [24]. Our simulations make use of a dynamic meshing methodology that can accommodate a changing shape as a result of the oscillatory motion of the assembly. To achieve this, the entire computational domain is split into three distinct regions, namely, (1) a rigid region that moves with the assembly without any deformation, (2) a mesh-morphing region that is deformed and updated with each time step, and (3) a static mesh region that is stationary (viz., the mesh here does not change in time). A structured grid is generated in the domain—the grid consists of $\sim 35\,000$ nodes. Finally, we employ a time step of $\Delta t = 0.01$ s in our numerical simulations.

The dynamics corresponding to the two-way FSI between the flow and the elliptical cylinder-plate assembly is simulated using the two-dimensional unsteady incompressible Navier-Stokes (NS) equations for fluid flow given by

$$\frac{\partial u_i}{\partial x_i} = 0, \quad (1)$$

$$\frac{\partial u_i}{\partial t} + u_j \frac{\partial u_i}{\partial x_j} = -\frac{1}{\rho} \frac{\partial p}{\partial x_i} + \nu \frac{\partial^2 u_i}{\partial x_j \partial x_j}, \quad (2)$$

and an equation of motion for the assembly given by the following ordinary differential equation for a mass-spring-damper system:

$$m\ddot{y}(t) + c\dot{y}(t) + ky(t) = F_y(t). \quad (3)$$

Here, the position vector is $\mathbf{x} = (x_1, x_2) = (x, y)$, the velocity vector is $\mathbf{u} = (u_1, u_2) = (u, v)$, and the subscript $i = 1, 2$ on a quantity refers to a Cartesian component of a vector in the x and y directions, respectively. Furthermore, p , ρ , and ν are the pressure, fluid density, and fluid kinematic viscosity; t is time; y , \dot{y} , and \ddot{y} represent the displacement, velocity, and acceleration of the oscillating assembly in the transverse direction; m is the mass of the oscillating assembly; c is the structural damping coefficient; k is the spring stiffness; and $F_y(t)$ is the transverse fluid force acting on the assembly. Note that, for a two-dimensional problem, m , c , k , and F_y are defined per unit length.

The above governing equations are discretized using a finite-volume method, and the numerical calculations are carried out using the open-source computational fluid dynamics (CFD) package OpenFOAM version 4.1. Reformulated NS equations in the arbitrary Lagrangian Eulerian (ALE) framework are solved to simulate the flow dynamics affected by the oscillation of the assembly. To this purpose, the pimpleDyMFOam solver and the PIMPLE algorithm are employed which are characterized by second-order numerical discretization schemes [2]. Moreover, Eq. (3) is solved using the Newmark- β methodology (with $\gamma = 0.5$ and $\beta = 0.25$) to provide the transverse oscillatory motion of assembly at every time step.

For reference, we define a number of nondimensional parameters in the subsequent analysis. The Reynolds number is defined as $\text{Re} \equiv UD/\nu$; the reduced velocity is defined as $U_r \equiv U/(f_n D)$, where $f_n \equiv (k/m)^{1/2}/(2\pi)$ is the structural natural frequency; the lift and drag coefficients are given by $C_L \equiv 2F_y/(\rho U^2 D)$ and $C_D \equiv 2F_x/(\rho U^2 D)$, where F_x and F_y are the components of fluid force in the x and y directions, respectively. The numerical simulations are conducted for a laminar flow ($\text{Re} = 100$) past an elliptical cylinder-plate assembly with a reduced mass $m^* = 10$ (viz., ratio of the assembly mass to the displaced fluid mass) and a zero structural damping (viz., $\zeta \equiv c/[2\pi(km)^{1/2}] = 0$). It should be noted that the spring constant k is varied to obtain the range of values of the reduced velocity (viz., $U_r = 2$ to 30) used in this paper. Additional dimensionless quantities employed in this investigation include the dimensionless transverse displacement $Y \equiv y/D$ and the dimensionless time $\tau \equiv tU/D$. Note that the dimensional time t has the same numerical value as τ because $D = 1$ m and $U = 1$ m s^{-1} in our numerical simulations.

III. RESULTS AND DISCUSSIONS

The FIV of various elliptical cylinder-plate assemblies with $0.5 \leq \text{AR} \leq 2$ and $L_{\text{SP}}/D = 0.75$ is analyzed in detail—the analysis here includes the vibration response in terms of amplitude, frequency and fluid forces, the branching behavior, as well as the dynamical characteristics of the vibrations in the synchronization and nonsynchronization branches. Furthermore, we investigate the transverse FIV of an elliptical cylinder-plate assembly with a longer splitter-plate length, namely, $L_{\text{SP}}/D = 2.5$.

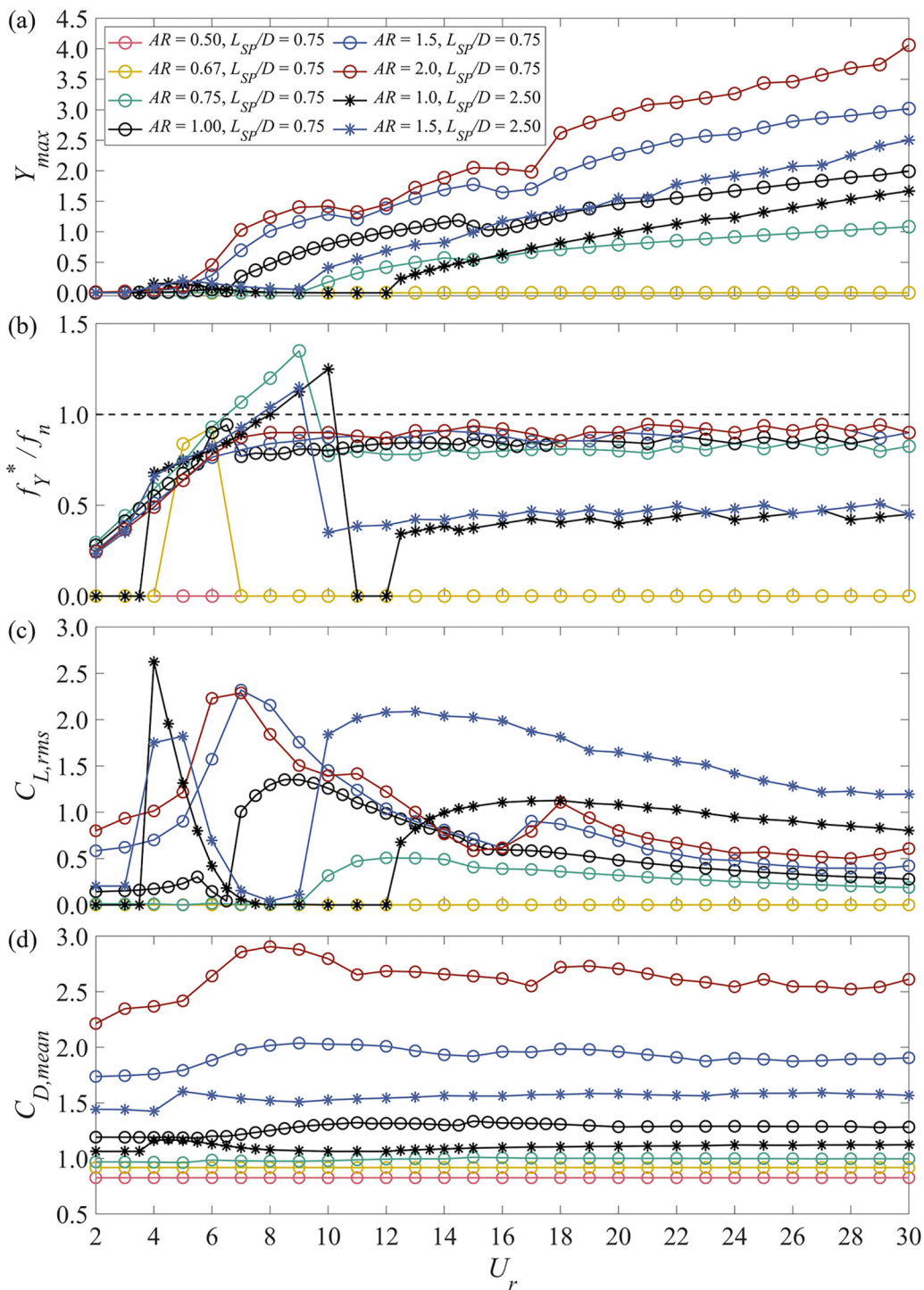


FIG. 3. Effect of the aspect ratio ($0.5 \leq AR \leq 2.5$) on the flow-induced vibration (FIV) of an elliptical cylinder-plate assembly with two different splitter-plate lengths ($L_{SP}/D = 0.75$ and 2.5). The following quantities of interest are shown: (a) the maximal transverse displacement Y_{max} , (b) the normalized dominant frequency f_Y^*/f_n of the transverse displacement, (c) the root-mean-square lift coefficient $C_{L,rms}$, and (d) the mean drag coefficient $C_{D,mean}$ as a function of the reduced velocity U_r .

A. Vibration response

Figure 3 compares the free oscillation induced on an elliptical cylinder-plate assembly for various ARs ($AR = 0.5\text{--}2$) and for two splitter-plate lengths ($L_{SP}/D = 0.75$ and 2.5)—the quantities of interest displayed here include the maximum transverse displacement Y_{\max} , the frequency ratio f_Y^*/f_n [where f_Y^* is the dominant frequency in the power spectral density (PSD) of Y], the root-mean-square lift coefficient $C_{L,rms}$, and the mean drag $C_{D,mean}$ coefficient exerted on the assembly by the fluid. An examination of this figure shows that all the assemblies experience an unlimited FIV in which Y_{\max} generally increases with U_r . Wu *et al.* [23] showed that the FIV mode (viz., whether self-limited or unlimited) was determined primarily by the splitter-plate length. Consequently, in this section, we focus on the influence of AR on the FIV of the assembly, where the fixed plate length is chosen to provoke an unlimited FIV.

For the assembly with $L_{SP}/D = 0.75$, we have investigated six values of AR in the range from 0.5 to 2. For the two smallest ARs (viz., $AR = 0.5$ and 0.67), it is evident that no oscillation occurs in the assembly—indeed, the amplitude response, the characteristic oscillation frequency, and the lift coefficient have values near zero [see Figs. 3(a)–3(c)], and the drag force is constant with respect to U_r [viz., $C_{D,mean} \approx 0.83$ and 0.92 for $AR = 0.5$ and 0.67 , respectively, on examination of Fig. 3(d)]. Even so, the dynamical behavior of the assembly with $AR = 0.5$ slightly differs from that with $AR = 0.67$ —their frequency responses in Fig. 3(b) show that $f_Y^*/f_n \approx 0$ for $AR = 0.5$ over the entire reduced-velocity range $U_r = 2\text{--}30$, whereas that for $AR = 0.67$ exhibits a rapid increase to $f_Y^*/f_n \approx 1$ over $U_r = 5\text{--}6$.

For $AR \geq 0.75$, an unlimited oscillation can be induced in the elliptical cylinder-plate assembly. An increasing AR provokes oscillations in two aspects, namely, the onset of FIV occurs at lower values of U_r (e.g., the onset is $U_r = 9, 6.5, 6,$ and 5 for $AR = 0.75, 1, 1.5,$ and 2 , respectively), and the maximum transverse displacement increases with AR, as is evident on a careful perusal of the amplitude responses in Fig. 3(a). In stark contrast, the influence of AR on the frequency response appears to be less obvious—indeed, it can be seen that f_Y^*/f_n varies only over a small range from 0.8 to 0.95 for AR varying from 0.75 to 2 [cf. Fig. 3(b)]. In Fig. 3(c), the lift force acting on the assembly attains a maximum value around the onset velocity and gradually decreases with U_r . Moreover, $C_{L,rms}$ is sensitive to the changes in the AR—the maximum lift coefficient increases by approximately a factor of three (e.g., from 0.5 to 1.4) as AR increases from 0.75 to 1, while this increase becomes slower (e.g., from 1.4 to 2.3) for AR increasing from 1 to 2. Unlike the lift force, the maximum drag force increases proportionally with AR, namely, the maximum value of $C_{D,mean}$ is 1, 1.3, 2, and 2.6 for $AR = 0.75, 1, 1.5,$ and 2 , respectively [cf. Fig. 3(d)]. Finally, it is noted that $C_{D,mean}$ is basically constant over $U_r = 2\text{--}30$.

The unlimited FIV response of an elliptical cylinder-plate assembly with a larger splitter-plate length of $L_{SP}/D = 2.5$ is also exhibited in Fig. 3 for $AR = 1$ and 1.5 . The effect of AR on the vibration response of the assembly is like that for $L_{SP}/D = 0.75$. The major difference for the case $L_{SP}/D = 2.5$ is the higher onset of FIV (viz., $U_r = 12$ and 9 for $AR = 1$ and 1.5 , respectively) and the lower dominant oscillation frequency ($f_Y^*/f_n = 0.43$ and 0.45 for $AR = 1$ and 1.5 , respectively). The analysis conducted here implies that increasing AR leads to a slight increase in the f_Y^*/f_n , whereas increasing L_{SP}/D has precisely the opposite effect, namely, that of significantly reducing f_Y^*/f_n .

Following from this analysis and some results reported by Wu *et al.* [23], the influence of AR on the self-limited and unlimited FIV of an elliptical cylinder-plate assembly can be summarized as follows. A self-limited FIV in the assembly is strengthened as AR increases at least over the range of $AR = 0.75\text{--}1.5$. However, the effective U_r range is reduced for $AR = 2$ owing to the absence of a nonsynchronization branch in the amplitude response. In contrast, for the unlimited FIV in the assembly, both the oscillation amplitude and the effective U_r range increase monotonically with AR—this effect is independent of the splitter-plate length provided, of course, that the length can provoke an unlimited FIV response in the assembly.

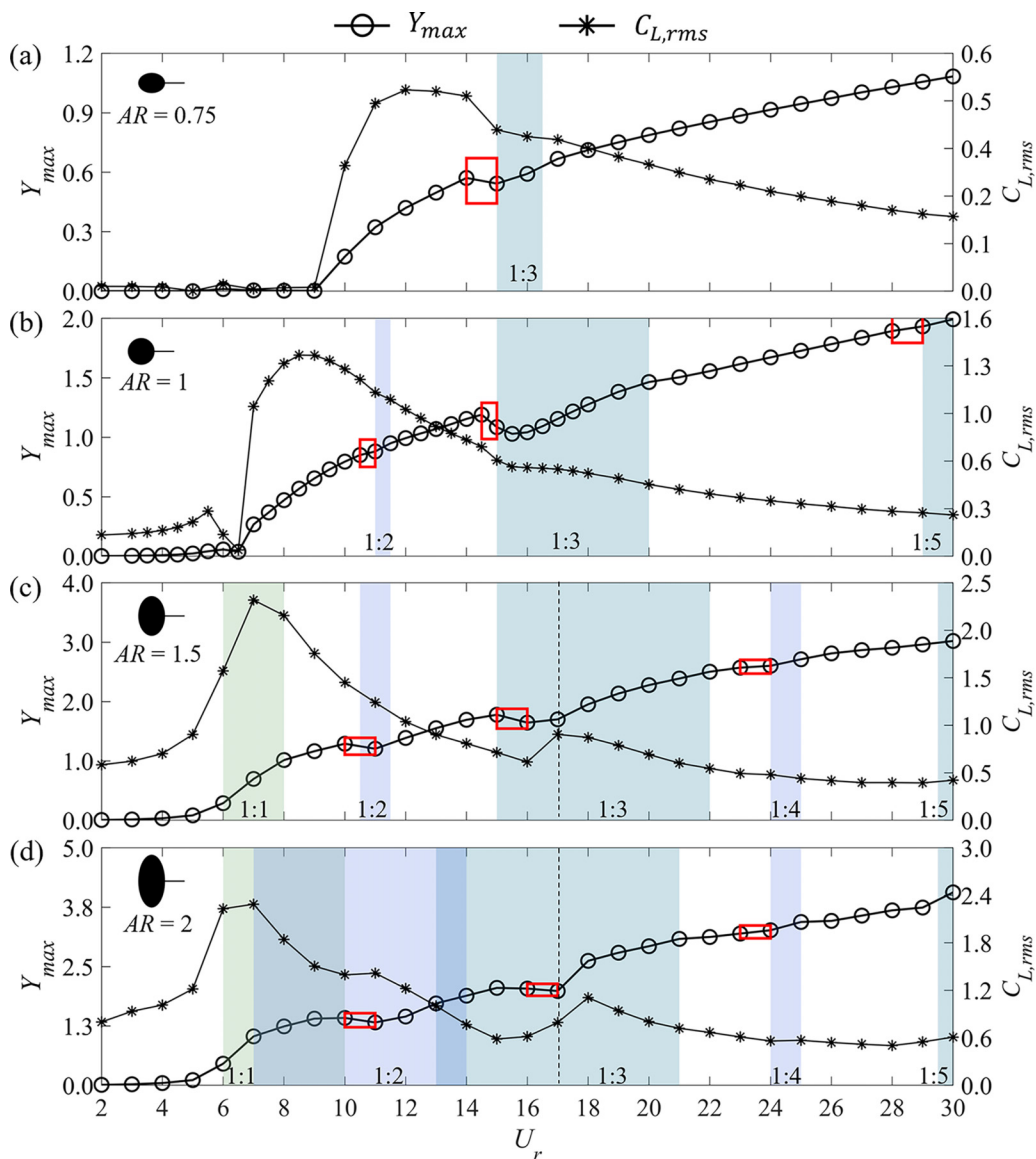


FIG. 4. Branching behavior of an unlimited flow-induced vibration (FIV) response provoked on an elliptical cylinder-plate assembly with various aspect ratios (ARs) and a fixed splitter-plate length $L_{SP}/D = 0.75$. The maximal transverse displacement Y_{max} (left vertical axis) and the root-mean-square lift coefficient $C_{L,rms}$ (right vertical axis) are plotted as a function of the reduced velocity U_r for ARs of (a) 0.75, (b) 1, (c) 1.5, and (d) 2. The synchronization branches are shaded in different colors. The kinks (discontinuity of the slope) in the amplitude response are delineated by the red boxes.

B. Branching behavior

The branching behavior of the unlimited FIV provoked on an elliptical cylinder-plate assembly with $L_{SP}/D = 0.75$ and ARs ranging from 0.75 to 2 are exhibited in Fig. 4. The corresponding PSD isopleths of Y and C_L as a function of U_r and the normalized frequency—either f_Y/f_n associated with Y or f_{C_L}/f_n associated with C_L —are displayed in Figs. 5 and 6, respectively. The individual

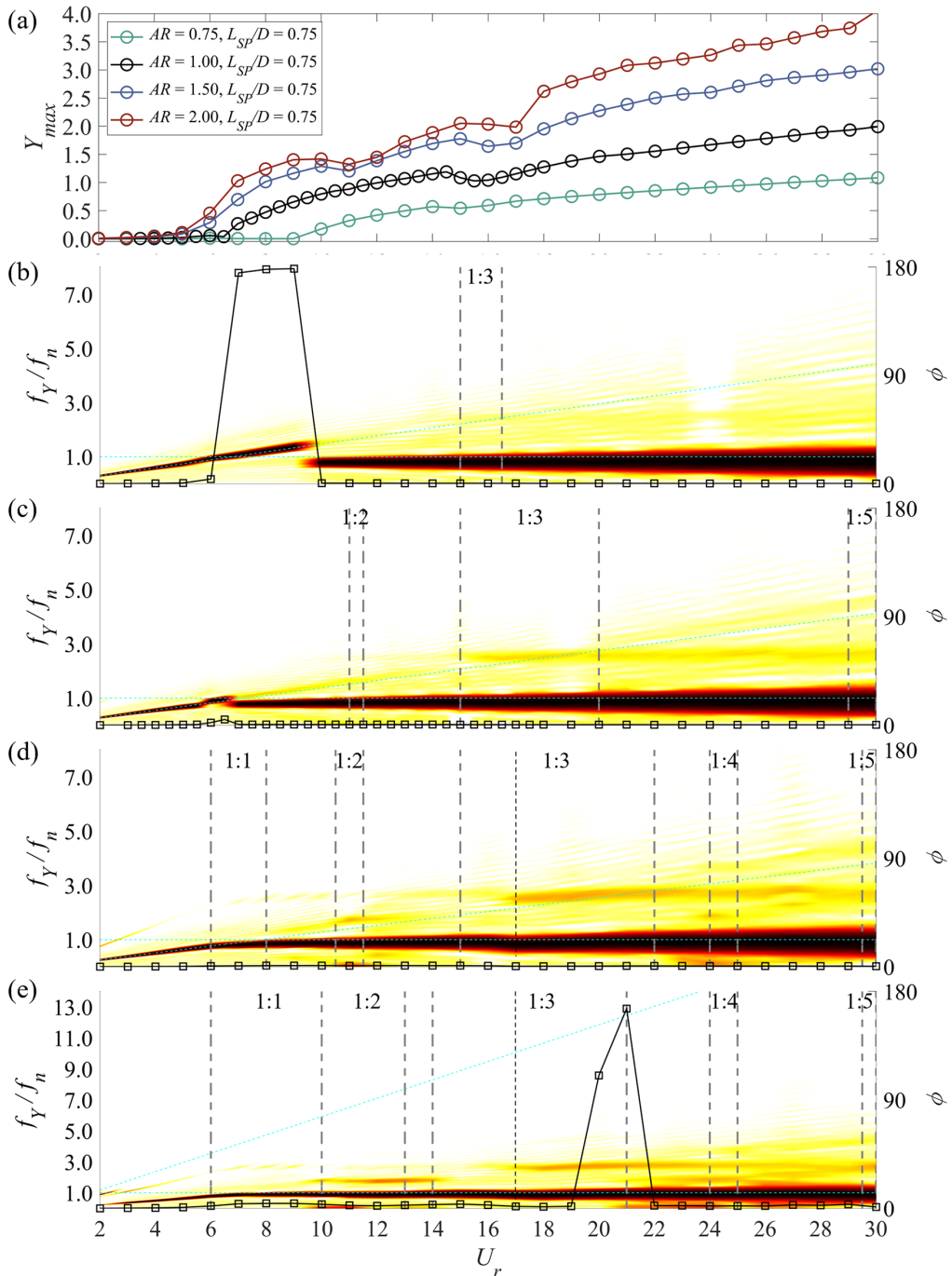


FIG. 5. (a) The maximum transverse displacement Y_{max} as a function of the reduced velocity U_r for an elliptical cylinder-plate assembly with aspect ratios (ARs) of 0.75–2 and a splitter-plate length $L_{SP}/D = 0.75$. The normalized power spectral density isopleths (logarithmic scale) of Y exhibited as a function of f_y/f_n and U_r for ARs of (b) 0.75, (c) 1, (d) 1.5, and (e) 2. The vertical dashed lines delineate the boundaries of synchronization regimes; the horizontal dashed line corresponds to $f_y/f_n = 1$; the diagonal dashed lines represent the vortex-shedding frequency of the stationary assembly; and the solid lines with squares correspond to the phase difference ϕ ($^\circ$) between Y and C_L .

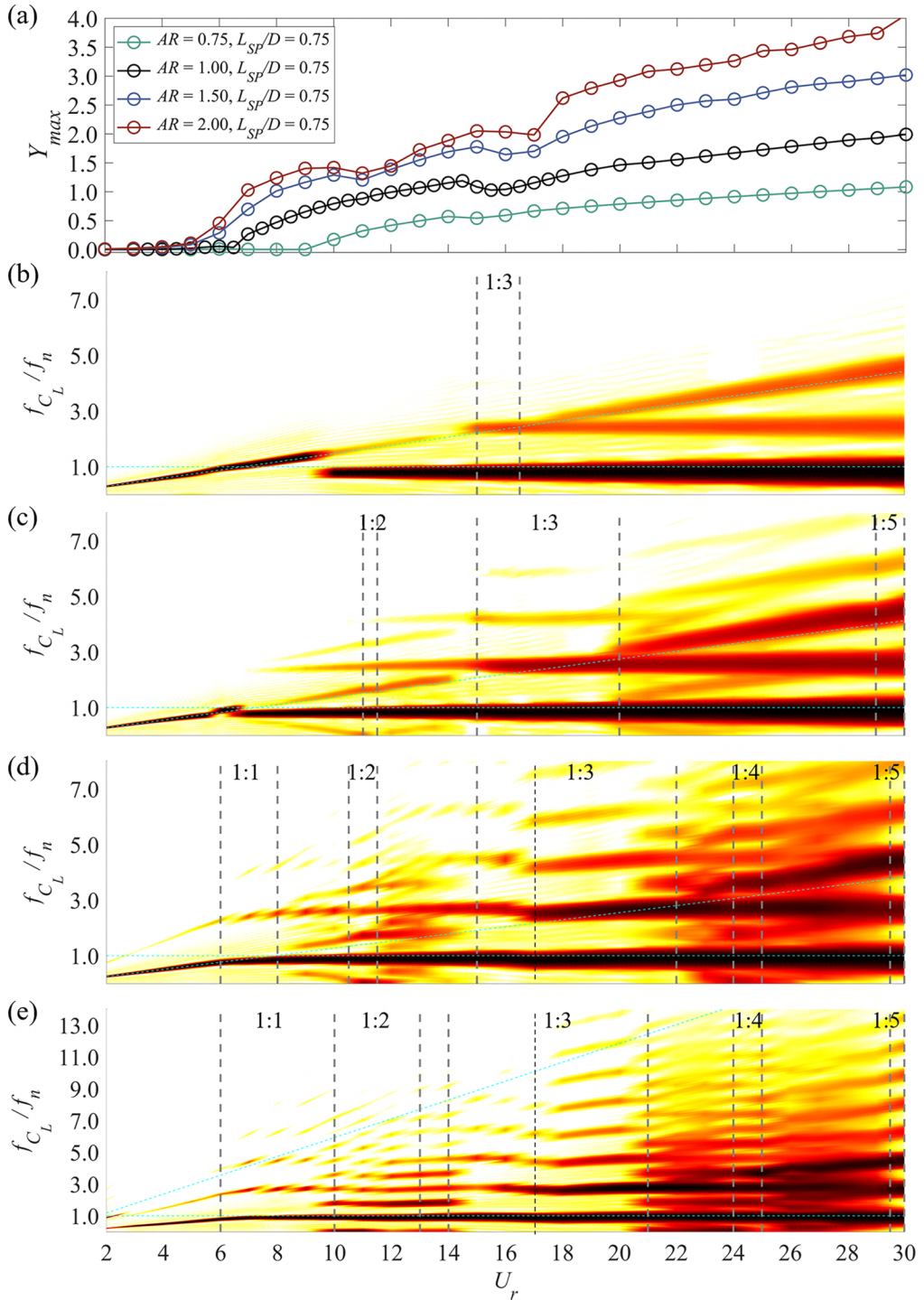


FIG. 6. (a) The maximum transverse displacement Y_{max} and the normalized power spectral density isopleths of C_L for an elliptical cylinder-plate assembly with a constant splitter-plate length of $L_{SP}/D = 0.75$ and various aspect ratios (ARs) of (b) 0.5, (c) 1, (d) 1.5, and (e) 2. Other notations used here are the same as those described in the caption of Fig. 5.

power spectra of the time series $Y(t)$ or $C_L(t)$ at each value of U_r are calculated, and these results are composed into a single plot to create the PSD isopleths that are shown here [4,12].

For the oblate ($AR < 1$) elliptical cylinder-plate assembly with $AR = 0.75$, it is seen that only one odd-multiple synchronization is present within the unlimited oscillation range—more specifically, $f_Y^*/f_{C_L}^* = 1:3$ at $U_r = 15$ – 16.5 whose onset is signalled by a kink in the amplitude response [delineated by the red box in Fig. 4(a)]. As a consequence, this assembly experiences a pure galloping response. The PSD isopleths of Y and C_L exhibit a simple form. More precisely, the dominant frequency of $Y(t)$ occurs at $f_Y^*/f_n = 0.8$ in the galloping regime [see Fig. 5(b)], whereas C_L exhibits an evident third-harmonic at $f_{C_L}^*/f_n = 2.4$ to give a 1:3 synchronization branch. Moreover, the harmonic frequencies in the oscillations of C_L gradually increase to higher order thereafter with U_r , as is evident from a perusal of Fig. 6(b). From this behavior, it is reasonable to suggest that a 1:5 synchronization branch may be present in the galloping regime at larger values of the reduced velocity than considered herein.

In comparison with an oblate elliptical cylinder-plate assembly, a circular cylinder-plate assembly exhibits more synchronization branches in the amplitude response that occur over a wider reduced-velocity range. More precisely, these regimes correspond to $f_Y^*/f_{C_L}^* = 1:2$, 1:3, and 1:5 at $U_r = 11$ – 11.5 , 15–20, and 29–30, respectively. The onset of each branch is signalled by a kink in the amplitude response, as is evident from an examination of Fig. 4(b). Note that there are small oscillations with $Y/D \approx 0.05$ at about $U_r = 6$ —this corresponds to the initial stage of a VIV that has not attained lock-in [22]. Consequently, the unlimited FIV response of a circular cylinder-plate assembly still consists primarily of galloping. In addition to the fundamental frequency of $f_Y^*/f_n \approx 0.85$, a third harmonic gradually emerges at $U_r \geq 16$ in the power spectrum of Y , as is evident in Fig. 5(c). In contrast, the C_L power spectrum exhibits a more complex harmonic structure—only odd harmonics are present in the odd (1:3 and 1:5) synchronization branches, whereas both odd and even harmonics are present in the even (1:2) synchronization branch.

For a prolate ($AR > 1$) elliptical cylinder-plate assembly with $AR = 1.5$ and 2, the most striking branching characteristic is that a 1:1 synchronization branch (i.e., lock-in) corresponding to the VIV regime is present at a lower value of U_r . This branch is succeeded at larger U_r by several high-order synchronization branches with $f_Y^*/f_{C_L}^* = 1:2$, 1:3, 1:4, and 1:5 in the galloping regime. Consequently, these assemblies experience an integrated VIV and galloping response. As is evident from Fig. 4(c), the five synchronization branches are separated from each other. Furthermore, the onset of the 1:2, 1:3, and 1:4 synchronization branches is signalled by a kink in the amplitude response. We note that the occurrence of the kink here depends not only on a sudden change in the slope of the amplitude plot but also on the appearance of a synchronization branch. A further and more detailed discussion of the kink in the amplitude response of a cylinder-plate assembly can be found in a previous study [22].

For the assembly with $AR = 2$ shown in Fig. 4(d), the first three synchronization branches are integrated with one another without any clear-cut boundaries between them (viz., $f_Y^*/f_{C_L}^* = 1:1$, 1:2, and 1:3 at $U_r = 6$ – 7 , 10–13, and 14–21, respectively). Consequently, two transition regions are present, namely, $U_r = 7$ – 10 between the 1:1 and 1:2 synchronizations and $U_r = 13$ – 14 between the 1:2 and 1:3 synchronizations. These transition regimes are identified by their distinctive vortex-shedding patterns which will be discussed in greater detail in Sec. III C 2.

Another interesting feature of the branching behavior for a prolate elliptical cylinder-plate assembly is that the 1:3 synchronization branch appears to be further split into two parts. The first subbranch— $U_r = 15$ – 17 for $AR = 1.5$ and $U_r = 14$ – 17 for $AR = 2$ —is characterized by three properties, namely, a near constant Y_{\max} as a function of U_r , the presence of a single frequency in the Y power spectrum, and the existence of a number of weaker and lower-order harmonic components in the C_L power spectrum. In marked contrast, the second subbranch (viz., $U_r = 17$ – 22 for $AR = 1.5$ and $U_r = 17$ – 21 for $AR = 2$) is characterized by an increase in the Y_{\max} as a function of U_r , the presence of a third harmonic in the Y power spectrum, and the existence of stronger and higher-order harmonic components in the C_L power spectrum. The subdivision of the 1:3 synchronization branch

is closely associated with the transition in the vortex-shedding patterns in this regime—this will be investigated in greater detail in Sec. III C 2.

C. Synchronization characteristics

The influence of AR on the dynamical characteristics and the vortex-shedding modes within the synchronization branches in the amplitude response of an elliptical cylinder-plate assembly is investigated in this section. To this purpose, we analyze the behavior of the oscillatory time series of Y and C_L .

1. Lock-in regime

Figure 7 compares the dynamic characteristics and vortex-shedding patterns in the 1:1 synchronization branch for an elliptical cylinder-plate assembly with $AR = 1.5$ and 2 at $U_r = 6$ as well as in the transition regime that occurs between the 1:1 and 1:2 synchronizations for the assembly with $AR = 2$ at $U_r = 7-8$.

As shown in Figs. 7(a)–7(c), $Y(t)$ consists of a periodic sinusoidal variation with one fundamental frequency—this is reflected in the presence of a circular limit cycle in the $Y-Y'$ phase plane. Increasing AR results in a nonsinusoidal waveform for $C_L(t)$, and this manifestation is associated with the more complex shapes of the phase portraits of $C_L(t)$ [red curve in Fig. 7(bii)]. Moreover, the increasing number of harmonic components present in the PSD of $C_L(t)$ with increasing AR and/or U_r [cf. Figs. 7(aiv), 7(biv), and 7(civ)] are reflected in the increasing complexity of the corresponding Lissajous figures with AR and/or U_r [cf. Figs. 7(aiii), 7(biii), and 7(ciii)]. In the transition regime between the 1:1 and 1:2 synchronization branches for $AR = 2$ at $U_r = 8$, the temporal waveform of $C_L(t)$ is noticeably nonsinusoidal owing to the presence of a larger number of stronger harmonics in the corresponding power spectrum.

A careful inspection of Figs. 7(d) and 7(e) shows that the vortex-shedding pattern associated with the 1:1 synchronization branch is a 2S wake mode consisting of two counterrotating vortices (one with positive vorticity S_1 and the other with negative vorticity $-S_1$) that are shed alternately from one side to the other of the assembly during one oscillation cycle to form the so-called Kármán vortex street. Furthermore, the vortex shape is strongly dependent on the AR, namely, elliptically shaped vortices are evident at $AR = 1.5$, whereas vortices consisting of a vortex core with a trailing tail [marked using black circles in Fig. 7(e)] are present at $AR = 2$.

In the transition regime between the 1:1 and 1:2 synchronization branches for $AR = 2$, the vortex shedding exhibits some new characteristic features. In Fig. 7(f), it is evident that a large positive vortex S_1 is first shed at $t = 0$ (beginning of an oscillation cycle of period T), followed by the shedding of a small slender vortex with the same sign (designated here as T_1) at $t = T/4$ —this vortex appears to be the tail of the next positive vortex. A similar vortex-shedding pattern occurs in the next half-oscillation cycle, except that the shed vortices have a negative sign ($-S_1$ and $-T_1$). The wake flow dynamics exhibited in Fig. 7(g) is different—the vortex-shedding pattern here involves a large vortex and a small tail vortex with an opposite sign that are shed together as a pair—more precisely, $(-S_1, T_1)$ and $(S_1, -T_1)$ are shed in one oscillation cycle. Moreover, the large vortices $-S_1$ and S_1 are not elliptically shaped as those in Fig. 7(f) but instead have a long tail. This dramatic change in the vortex-shedding pattern is only due to the marginally greater value of $U_r = 8$ in Fig. 7(g). It is evident that, in the transition regime, four vortices are shed in total in each oscillation cycle—these vortices have the characteristic vortex-tail pattern where the tail is smaller and possesses a weaker vorticity than that of the primary vortex. In view of this, we identify the wake mode in the transition regime as a quasi-2S mode.

2. Odd-multiple synchronization in the galloping regime

Figures 8 and 9 display the dynamical characteristics and wake modes associated with the odd-multiple (1:3) synchronization branch for elliptical cylinder-plate assemblies with $AR = 0.75-2$.

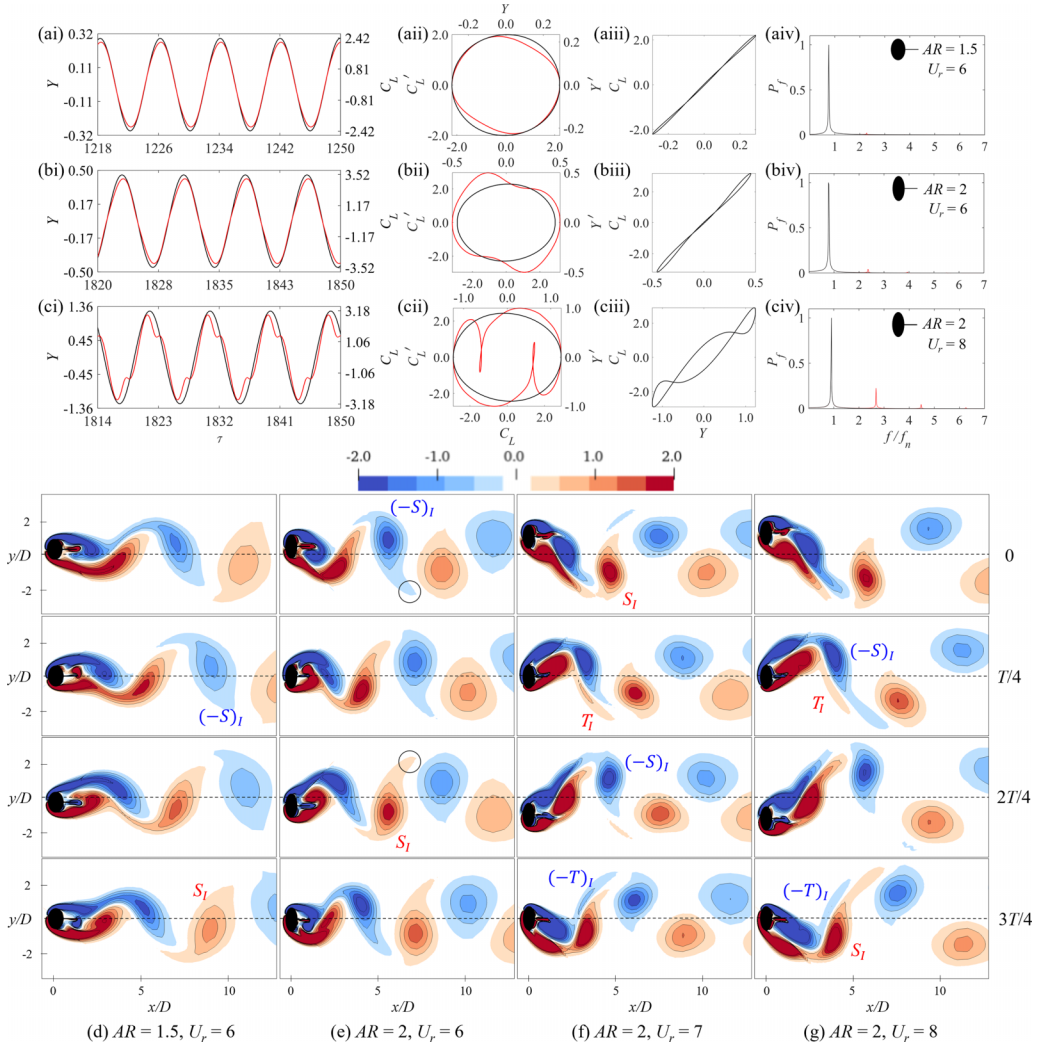


FIG. 7. Dynamical characteristics of the 1:1 synchronization branch (viz., lock-in) for an elliptical cylinder-plate assembly with aspect ratios (ARs) of (a) $AR = 1.5$ and (b) $AR = 2$ at $U_r = 6$ and of the transition regime between the 1:1 and 1:2 synchronization branches for (c) $AR = 2$ at $U_r = 8$. The four columns of panels in (a)–(c) exhibit the time series $Y(t)$ and $C_L(t)$, the phase portraits of $Y-Y'$ and $C_L-C'_L$, the Lissajous figures $Y-C_L$, and the power spectra of Y and C_L . In these plots, the results for Y and C_L are shown as the black and red curves, respectively. The evolution of the instantaneous vorticity field during one oscillation cycle with period T is displayed for (d) $AR = 1.5$ at $U_r = 6$, (e) $AR = 2$ at $U_r = 6$, (f) $AR = 2$ at $U_r = 7$, and (g) $AR = 2$ at $U_r = 8$. The 2S mode is identified in the 1:1 synchronization branch and the quasi-2S mode in the transition regime.

Two representative values of the reduced velocity (i.e., $U_r = 16$ and 20) are selected for $AR = 1.5$ and 2 , which correspond to the two subbranches of the 1:3 synchronization branch.

To begin, we study the influence of AR on the 1:3 synchronization branch at $U_r = 16$. As evident from an inspection of Figs. 8(a)–8(c) and 8(e), increasing AR from 0.75 to 2 results in a more complex $C_L(t)$, a more irregular phase portrait of $C_L-C'_L$, and in the presence of a stronger third harmonic in the C_L power spectrum. In marked contrast, increasing AR has little influence on the comparable characteristics for $Y(t)$. The corresponding vortex-shedding patterns are displayed in

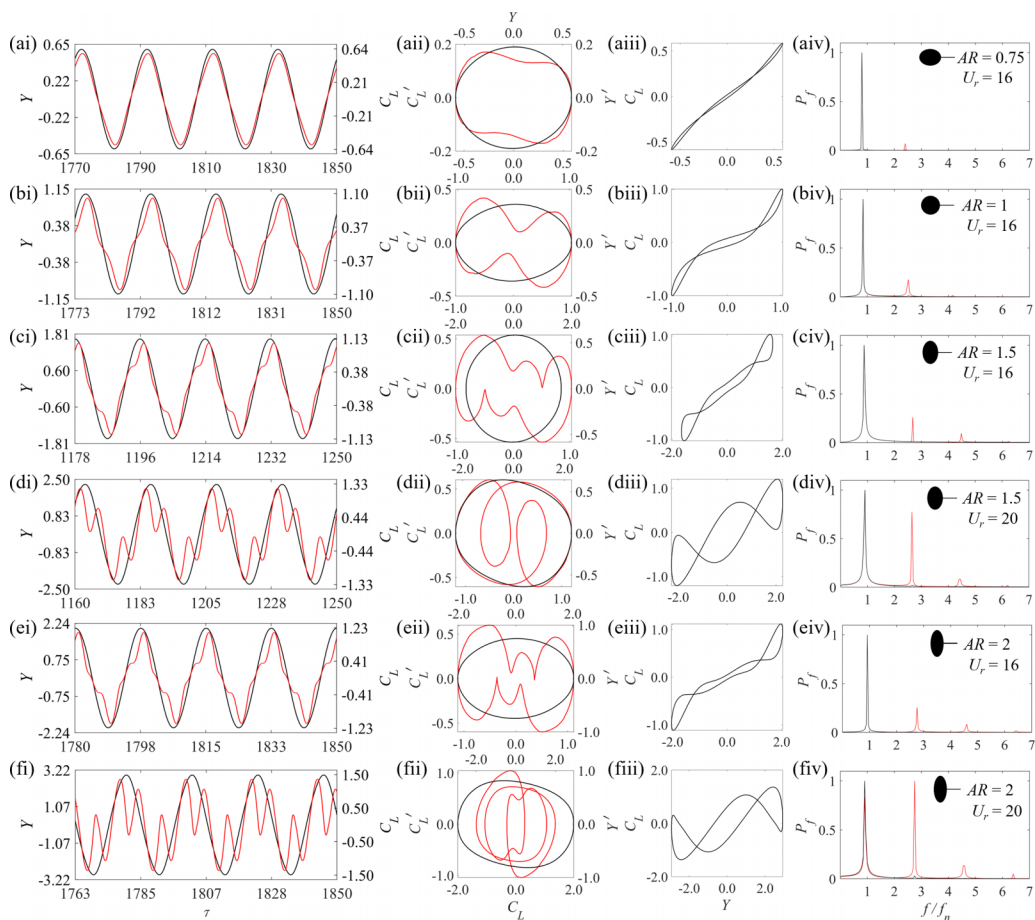


FIG. 8. Dynamical characteristics of the 1:3 synchronization branch for an elliptical cylinder-plate assembly with aspect ratios (ARs) of (a) 0.75, (b) 1, (c) and (d) 1.5, and (e) and (f) 2 at $U_r = 16$ and 20. The notation used here is the same as that described in the caption of Fig. 7.

Figs. 9(a)–9(d). A perusal of these figures shows that, for all values of AR studied herein, the vortex-shedding corresponds to a 2S mode that is shed three times over one oscillation cycle—so the 1:3 synchronization branch is associated with the $3 \times 2S$ wake mode. However, we note that some vortices that are shed from the assembly transition from an oblong shape (for $AR \leq 1$) to a more elongated shape (for $AR > 1$). More precisely, the vortices S_{II} and $-S_{III}$ [marked by the black box in Figs. 9(c) and 9(d)] shed from the assembly for $AR = 1.5$ and 2 become more slender and sinuous with increasing AR.

Next, we investigate the influence of U_r on the elliptical cylinder-plate assembly with $AR = 1.5$ and 2. As is evident on examination of Figs. 8(d)–8(f), increasing U_r from 16 to 20 results in the emergence of a strong third harmonic (with an amplitude comparable to that of the fundamental frequency) in the C_L spectrum. As a result, the corresponding $C_L(t)$ is characterized by multiple peaks of various amplitudes, and the associated phase portrait $C_L-C'_L$ exhibits a complex loop structure with the various loops intersecting with one another. A careful inspection of Fig. 9(e) shows that the vortex-shedding pattern adheres to a $3 \times (2S)$ mode—however, the vortices here are more strongly oriented in the vertical direction and consist of larger and more slender vortices (S_{II} , $-S_{III}$) owing to the larger value of U_r .

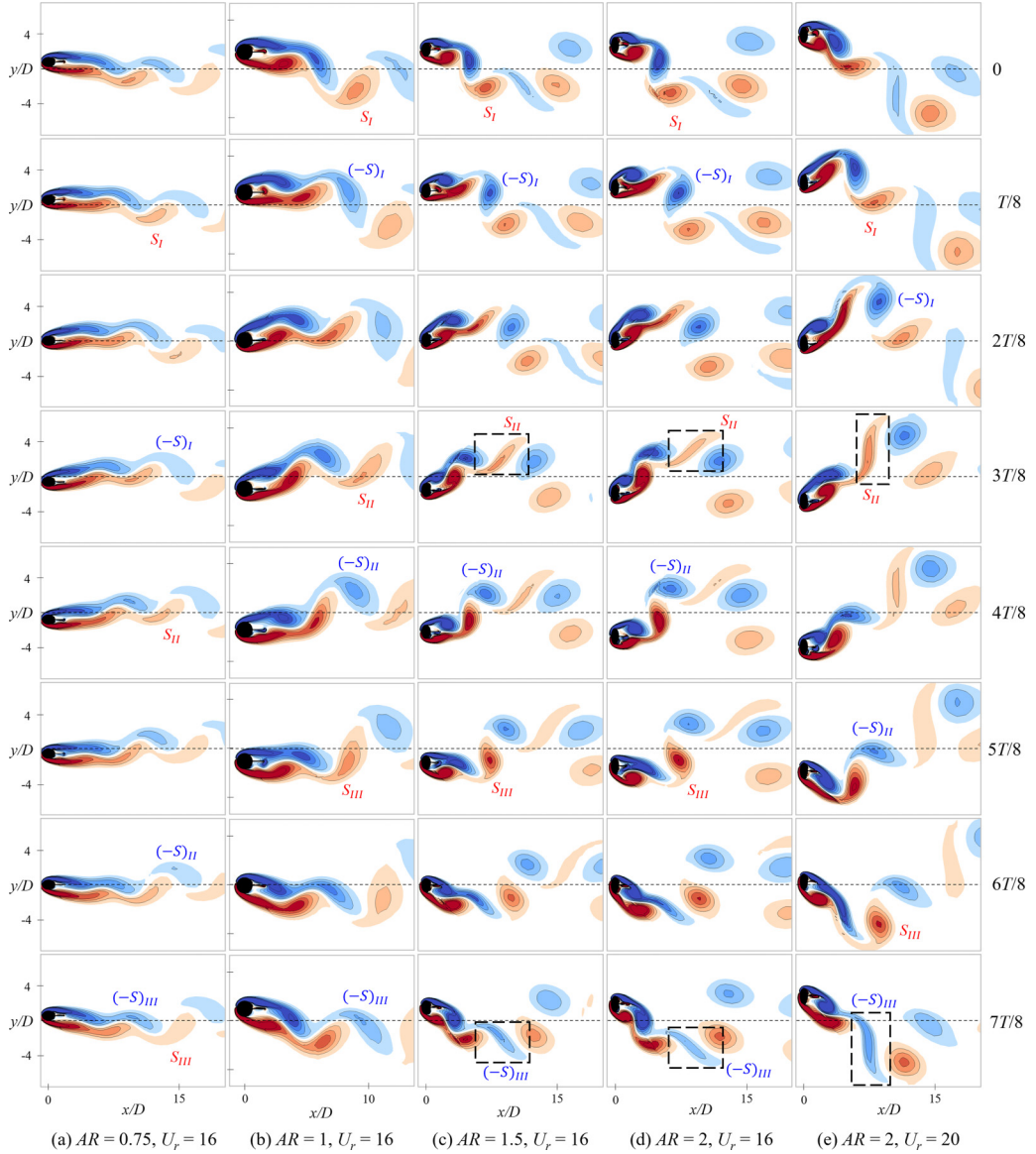


FIG. 9. The temporal evolution of instantaneous vorticity field over one oscillation cycle with period T in the 1:3 synchronization branch for an elliptical cylinder-plate assembly with aspect ratios (ARs) of (a) 0.75, (b) 1, (c) 1.5 and (d) and (e) 2 for $U_r = 16$ and 20. The 1:3 synchronization is associated with a $3 \times (2S)$ mode.

The vortex-shedding pattern associated with an elliptical cylinder-plate assembly reflects the nature of the oscillatory response of the assembly. To this point, the maximum transverse displacement increases significantly with AR for a given fixed reduced velocity (e.g., $Y_{\max}/D = 0.6, 1, 1.6,$ and 2 for $AR = 0.75, 1, 1.5,$ and 2 , respectively, at $U_r = 16$). This is probably due to the shedding of more slender vortices at larger ARs—these vortices are shed when near the maximum and minimum of the transverse displacement in each oscillation cycle [viz., the vortices S_{II} and S_{III} are respectively shed at $t = 3T/8$ and $t = 7T/8$ in the oscillation cycle, just before the occurrence of positive and negative peaks in Fig. 9(e)]. Furthermore, the value of Y_{\max} is almost constant in the first subbranch

of the 1:3 synchronization, whereas Y_{\max} increases with U_r in the second subbranch. This is true for an elliptical cylinder-plate assembly with $AR = 1.5$ and 2. This can be explained as follows. For these two ARs, the orientation of the slender vortices transitions from an oblique orientation to an almost vertical orientation (viz., parallel to the transverse direction) as U_r increases. The nearly constant Y_{\max} (in the first subbranch) will accordingly begin to increase with U_r after a critical U_r has been exceeded. This occurs at $U_r = 17$ for $AR = 1.5$ and 2. As a result, the 1:3 synchronization branch is divided into two characteristic subbranches as noted previously.

Figure 10 exhibits the dynamical characteristics of the 1:5 synchronization branch for the elliptical cylinder-plate assembly with various ARs. For the C_L power spectrum, the fifth harmonic is significant, and the seventh harmonic is evident—this complex power spectrum is associated with the more irregular temporal variations in $C_L(t)$ and the loop system in the phase portrait $C_L-C'_L$. An increase in AR has a similar effect on the 1:5 synchronization to that on the 1:3 synchronization described above. Correspondingly, the wake mode is identified as $5 \times (2S)$ (viz., the 2S mode is shed five times over one oscillation cycle).

3. Even-multiple synchronization in the galloping

Figures 11 and 12 present the 1:2 and 1:4 synchronization branches for an elliptical cylinder-plate assembly with $AR = 1, 1.5,$ and 2 at $U_r = 11$ and 24. These figures also exhibit the transition regime between the 1:2 and 1:3 synchronizations for $AR = 2$ at $U_r = 13$ –14. The most remarkable aspect of an even-multiple synchronization is that, in contrast with the antisymmetric odd-multiple synchronizations described in Sec. III C 2, the characteristic plots of the lift coefficient and flow patterns are asymmetric. This is evident from the asymmetric $C_L(t)$ about the $C_L = 0$ line, the asymmetric phase-plane portraits $C_L-C'_L$, and the asymmetric Lissajous figures $Y-C_L$ about the origin. Other aspects of the even-multiple synchronizations are like those described in Secs. III C 1 and III C 2. For example, increasing AR produces higher and stronger harmonic frequencies in the $C_L(t)$ spectrum but has a negligible effect in that of $Y(t)$. In addition, the vortex-shedding modes for the 1:2 and 1:4 synchronization branches are $2 \times (2S)$ [see Figs. 11(e)–11(g)] and $4 \times (2S)$ [see Figs. 12(c) and 12(d)], respectively.

The transition regime between the 1:2 and 1:3 synchronizations for an elliptical cylinder-plate assembly with $AR = 2$ occurs over $U_r = 13$ –14—this is determined following a careful analysis of the shape and number of vortices shed over one oscillation cycle. More precisely, at $U_r = 13$, a 2S mode (vortices S_I and $-S_I$) is observed in the first part of T . In the second part, an unusual flow pattern occurs, namely, the negative vortex $-S_{II}$ is followed by a same-signed tail vortex ($-T_I$), and subsequently, this is accompanied by the shedding of a positive vortex S_{II} [see Fig. 11(h)]. Consequently, five vortices are shed during one oscillation cycle at $U_r = 13$. This number is midway between the four vortices [i.e., $2 \times (2S)$] shed in the 1:2 synchronization and the six vortices [i.e., $3 \times (2S)$] shed in the 1:3 synchronization. At $U_r = 14$, the 2S mode is shed twice in the first part of T , which is followed in the second part by the shedding of a positive elliptically shaped vortex S_{III} and a negative tail vortex $-T_I$ [see Fig. 11(i)]. Although the total number of vortices shed during one oscillation cycle here is six, the vorticity associated with the last vortex is smaller than that in the 1:3 synchronization branch—so the transition branch occurs at $U_r = 14$.

In summary, the synchronization branch between the structural oscillation and the vortex shedding from the elliptical cylinder-plate assembly exhibits highly periodic dynamical characteristics—these can be either antisymmetric (odd-multiple) or asymmetric (even-multiple). For an unlimited FIV of the assembly, the vortex shedding in a synchronization branch generally conforms to an $n \times (2S)$ wake mode, where n is the ratio of the vortex-shedding frequency to the vibration frequency. The vortices in this wake mode are alternately shed from one side to the other. However, it is noted that tail vortices can occur in the transition regime between two synchronization branches. In marked contrast, the wake modes observed in the synchronization branch of a self-limited FIV are generally more complex (e.g., T+S, P+S) [23].

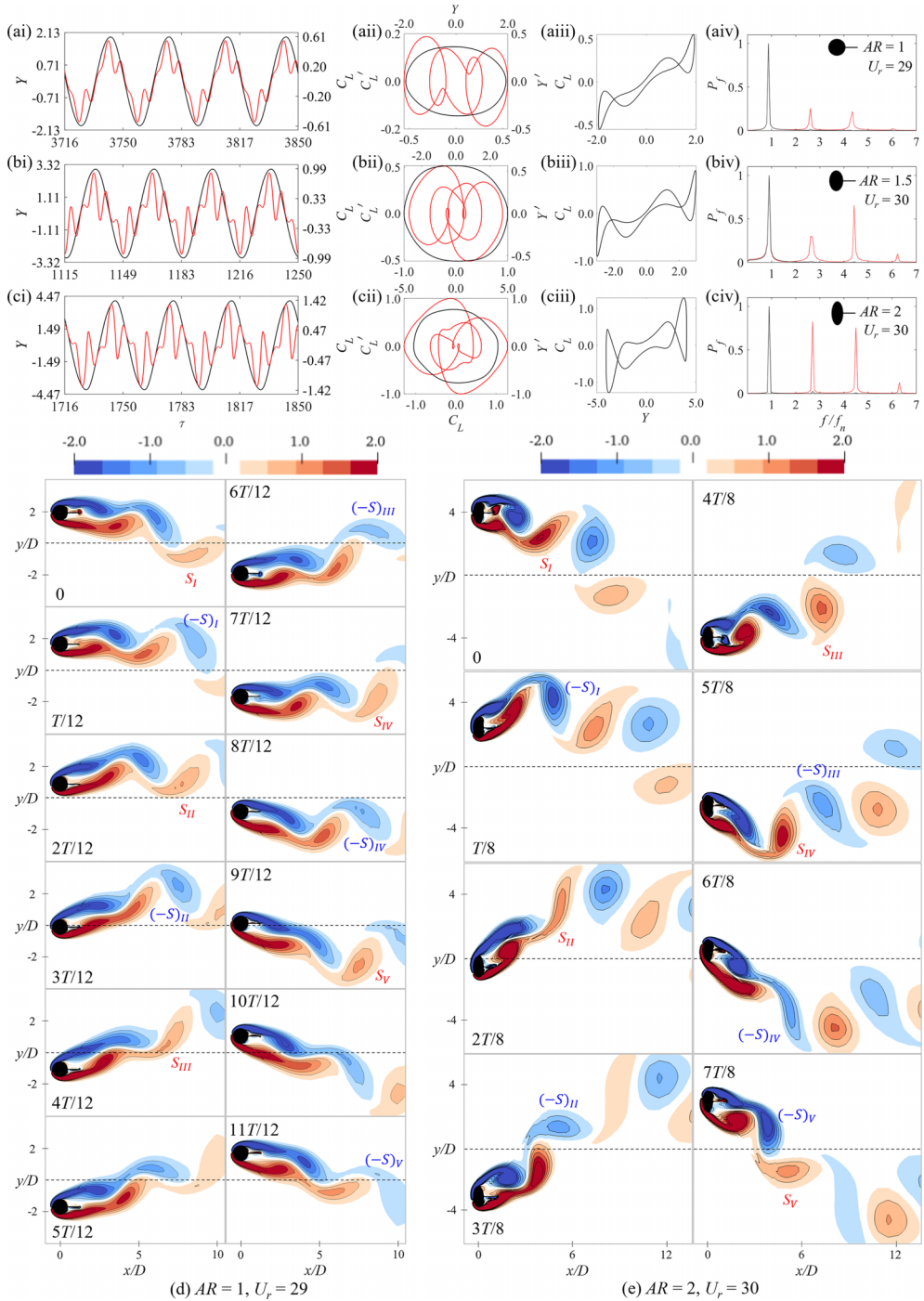


FIG. 10. Dynamical characteristics of the 1:5 synchronization branch for an elliptical cylinder-plate assembly with (a)–(c) aspect ratios $AR = 1, 1.5$ and 2 at $U_r = 29$ and 30 . The notation used here is the same as that described in the caption of Fig. 7. The vortex-shedding pattern over one oscillation cycle with period T is exhibited in (d) and (e) where a $5 \times (2S)$ wake mode is seen to be associated with the 1:5 synchronization branch.

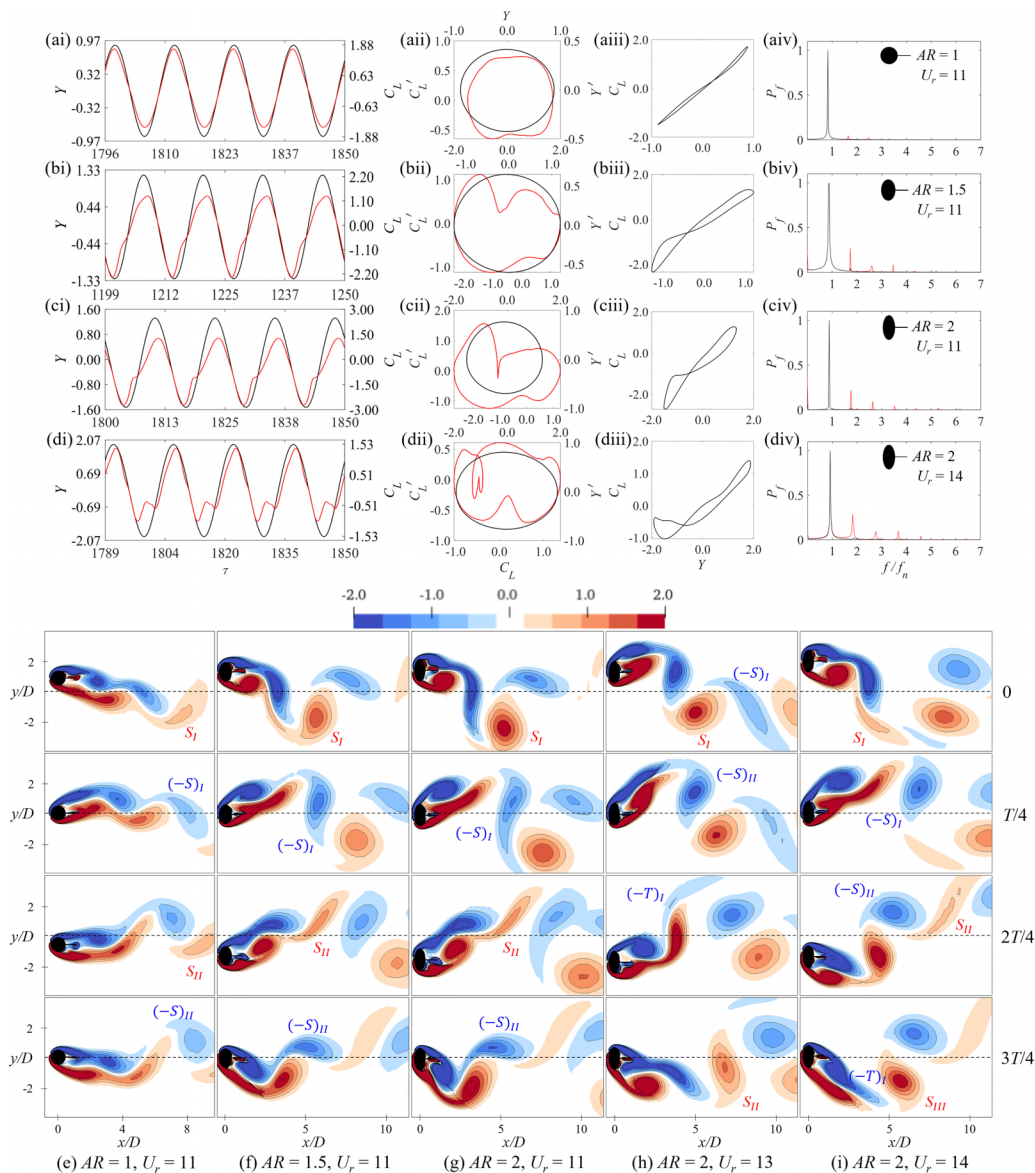


FIG. 11. Dynamical characteristics of the 1:2 synchronization branch for an elliptical cylinder-plate assembly with (a)–(c) aspect ratios $AR = 1, 1.5$, and 2 at $U_r = 11$. The transition regime between the 1:2 and 1:3 synchronizations for the assembly with (d) $AR = 2$ at $U_r = 14$. The notations used in (a)–(d) follow that given in the caption of Fig. 7. Temporal evolution of instantaneous vorticity field during one oscillation cycle for an assembly with (e)–(g) $AR = 1, 1.5$, and 2 at $U_r = 11$ and (h)–(i) $AR = 2$ at $U_r = 13$ and 14 . The 1:2 synchronization branch supports a $2 \times (2S)$ wake mode and the transition regime supports a quasi- $2 \times (2S)$ wake mode.

D. Nonsynchronization characteristics

In Fig. 4, it is evident that there exist regions between the synchronization branches in the amplitude response of an elliptical cylinder-plate assembly. These regions correspond to the nonsynchronization branches in the galloping regime. For $AR \leq 1.5$, the nonsynchronization regimes

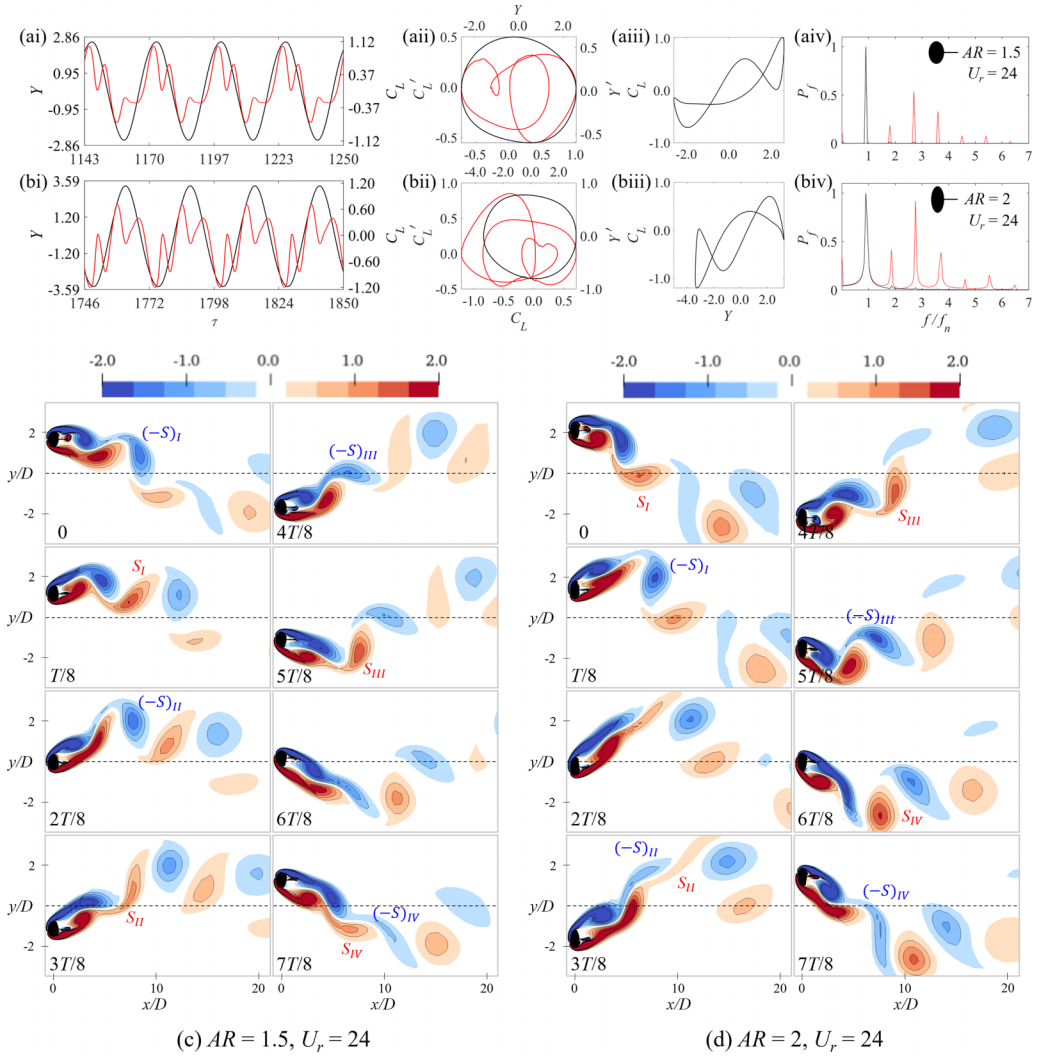


FIG. 12. Dynamical characteristics of the 1:4 synchronization branch for an elliptical cylinder-plate assembly with (a) aspect ratio $AR = 1.5$ and (b) 2 at $U_r = 24$. The notations used in (a) and (b) follow that given in the caption of Fig. 7. (c) and (d) Temporal evolution of instantaneous vorticity field during one oscillation cycle with a period T . The 1:4 synchronization branch supports a $4 \times (2S)$ wake mode.

account for a considerable proportion in the amplitude response—the U_r range associated with these branches is comparable with or even greater than that for the synchronization branches.

Figure 13 displays the power spectra of C_L for $6 \leq U_r \leq 30$ for an elliptical cylinder-plate assembly with $AR = 0.75-2$. These power spectra provide a comparison of the frequency content of the C_L power spectra associated with the synchronization (colored lines) and nonsynchronization (black lines) in the galloping regime. First, the assembly with larger AR is associated with a more complex frequency structure—this observation applies in both synchronization and nonsynchronization branches. Second, the frequency content is composed of a fundamental frequency and a number of odd (e.g., third and fifth) harmonics in the odd-synchronization branches (e.g., 1:1, 1:3, and 1:5). In contrast, both even and odd (e.g., second, third, fourth, and fifth) harmonics of the fundamental frequency are present in the even-synchronization branches (e.g., 1:2, 1:4).

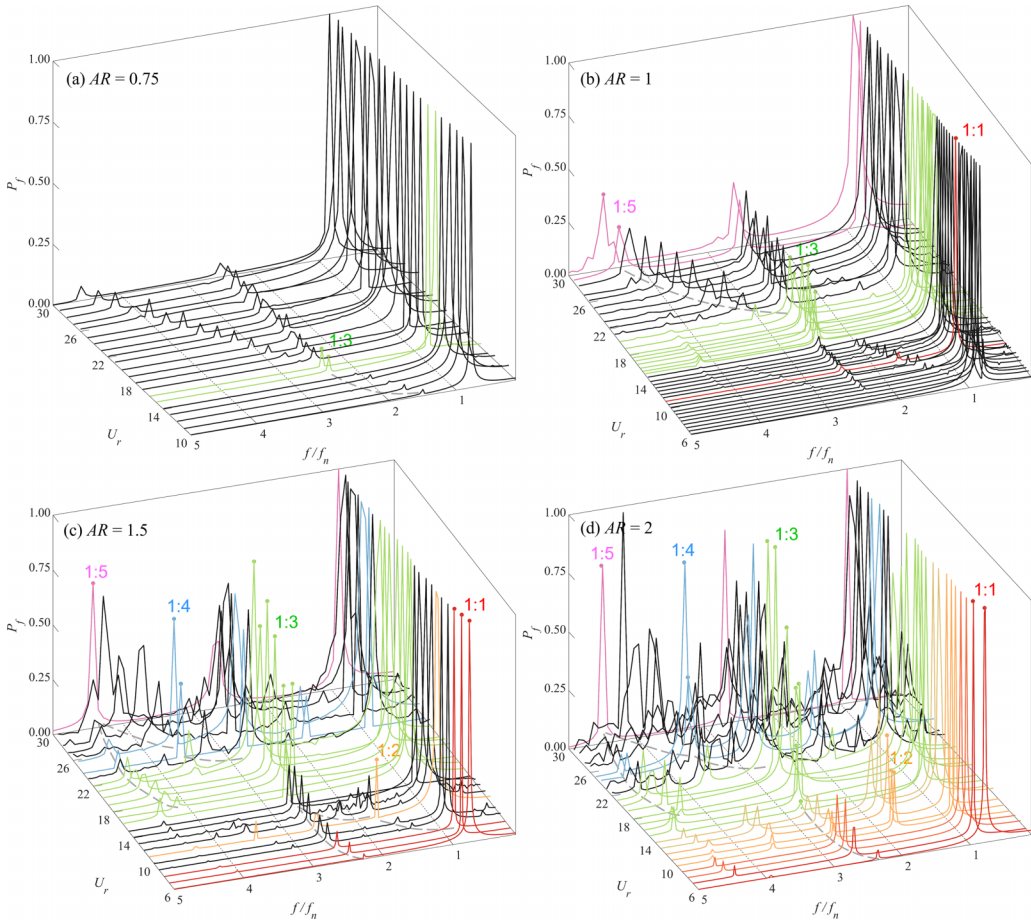


FIG. 13. The normalized power spectra of C_L at reduced velocities in the range from 6 to 30 for an elliptical cylinder-plate assembly with (a)–(d) aspect ratios $AR = 0.75, 1, 1.5,$ and 2 .

Additionally, the C_L spectra of the synchronization branch are essentially invariant (unchanged) as a function of U_r . In stark contrast, the C_L spectra vary with U_r in the nonsynchronization branch—ever higher-order harmonics emerge with increasing U_r , as is evident on a careful perusal of Figs. 13(a) and 13(b).

The harmonics in the C_L power spectra in two successive synchronization branches are seen to evolve in the nonsynchronization branch lying between these two branches (viz., a particular harmonic in the C_L power spectrum for the lower-order synchronization transitions to an associated harmonic in that for the next higher-order synchronization in the intervening non-synchronization branch). For example, in an elliptical cylinder-plate assembly with $AR = 1.5$ shown in Fig. 13(c), the fundamental frequency in the C_L power spectrum of the 1:1 synchronization branch evolves smoothly in the C_L power spectra through the nonsynchronization branch at $U_r = 9$ – 10 (see the single gray dashed line) to give the associated second harmonic in the C_L power spectrum of the 1:2 synchronization branch. Furthermore, the second and third harmonics in the C_L power spectrum of the 1:3 synchronization branch appear to both contribute to an associated harmonic in that of the 1:4 and 1:5 synchronization branches as it undergoes a smooth transition in the frequency content of the power spectra associated with the intervening nonsynchronization branches [see the pair of dashed gray lines in Fig. 13(c)]. In marked contrast, for an elliptical cylinder-plate assembly with

AR = 2 displayed in Fig. 13(d), there is no nonsynchronization branch between the 1:1, 1:2, and 1:3 synchronization branches.

The preceding analysis demonstrates that the frequencies in the C_L power spectrum corresponding to a nonsynchronization branch are not necessarily harmonics of a fundamental frequency—these frequencies are a signature of the underlying aperiodic dynamics in the branch. The typical phenomenon associated with the aperiodic dynamics is the presence of an amplitude modulation (or beating) in the $C_L(t)$ time series. Figure 14 provides an example of the aperiodic characteristics in the nonsynchronization branch—the signature is evident in the $C_L(t)$ time series, the phase portrait $C_L-C'_L$, and the Poincaré section for elliptical cylinder-plate assembly with various ARs and at a number of representative reduced velocities. Indeed, the $C_L(t)$ time series exhibits complex variations over a number of scales, the phase-plane portrait $C_L-C'_L$ consists of multiple overlapping and intersecting loops, and the Poincaré section is composed of a complex point set (rather than simply a single point)—these characteristics are indicative of the highly aperiodic nature of the dynamics in the nonsynchronization branch.

A few cases shown in Fig. 14 exhibit a quasiperiodic dynamical behavior (e.g., a period-doubling oscillation). For example, the dynamics in Fig. 14(c) corresponds to a period-3 beating for the amplitude of C_L , as is evident on inspection of the trajectory in the phase-space portrait $C_L-C'_L$ (like that seen in the periodic oscillations in the synchronization branch) and of the presence of three clusters of points in the corresponding Poincaré section. The dynamics displayed in Fig. 14(d) is also a period-3 oscillation, as evidenced by the fact that the $C_L(t)$ time series repeats every three oscillation cycles. In comparison with the $C_L(t)$ time series in Fig. 14(c), the corresponding time series in Fig. 14(d) is substantially more complex—indeed, the dynamics here corresponds to a larger AR = 1.5 at $U_r = 23$. The greater complexity in the time series for this case is reflected also in the greater complexity in the associated phase-plane portrait $C_L-C'_L$ and in a greater number of point clusters in the associated Poincaré section. The example shown in Fig. 14(f) is a period-5 oscillation. The $C_L(t)$ time series here exhibits temporal variations on multiple time scales. The remaining examples in Fig. 14 are associated with an aperiodic dynamics which can manifest a symmetric beating [e.g., Figs. 14(ai) and 14(bi)], a nonsymmetric beating [e.g., Fig. 14(ei)], or a completely irregular beating without a clear-cut (discernible) amplitude envelope [e.g., Fig. 14(gi)]. An increasing AR and/or reduced velocity is associated with a more nonlinear dynamics in the nonsynchronization branch.

Figure 15 displays the flow pattern over a number of consecutive oscillation cycles for an elliptical cylinder-plate assembly with $L_{SP}/D = 0.75$ and AR = 1.5 at $U_r = 28$. This flow pattern corresponds to a period-5 oscillation. An inspection of this pattern shows that the vortex shedding corresponds an $n \times (2S)$ wake mode. At $U_r = 28$, which is located in the nonsynchronization branch between the 1:4 and 1:5 synchronization branches, n can have a value of either four (cycles 2 and 4) or five (cycles 1, 3, and 5). A few nonelliptically shaped vortices are present during the vortex-shedding process (e.g., the elongated vortices delineated within the black box). The wake mode in cycle 6 (not shown here) is identical to that of cycle 1—this implies that a period-5 oscillation is associated with this vortex-shedding pattern.

E. Assembly with a longer splitter-plate

Sections III A–III D focus on how the AR of an elliptical cylinder-plate assembly affects the dynamical characteristics of the unlimited FIV response of the assembly. In accordance with Wu *et al.* [22,24,25], a longer splitter-plate can provoke VIV and galloping responses on a circular cylinder-plate assembly at small and large values of the reduced velocity, respectively. In this section, we investigate the dynamic characteristics associated with an elliptical cylinder-plate assembly with AR = 1 and 1.5 but with a longer splitter-plate of $L_{SP}/D = 2.5$.

Figure 16 shows a comparison of the branching behavior of an elliptical cylinder-plate assembly with $L_{SP}/D = 2.5$ for AR = 1 and 1.5. As shown in Fig. 16(a), a lock-in regime and three consecutive odd-multiple (i.e., 1:3, 1:5, and 1:7) synchronization branches that abut one another in the

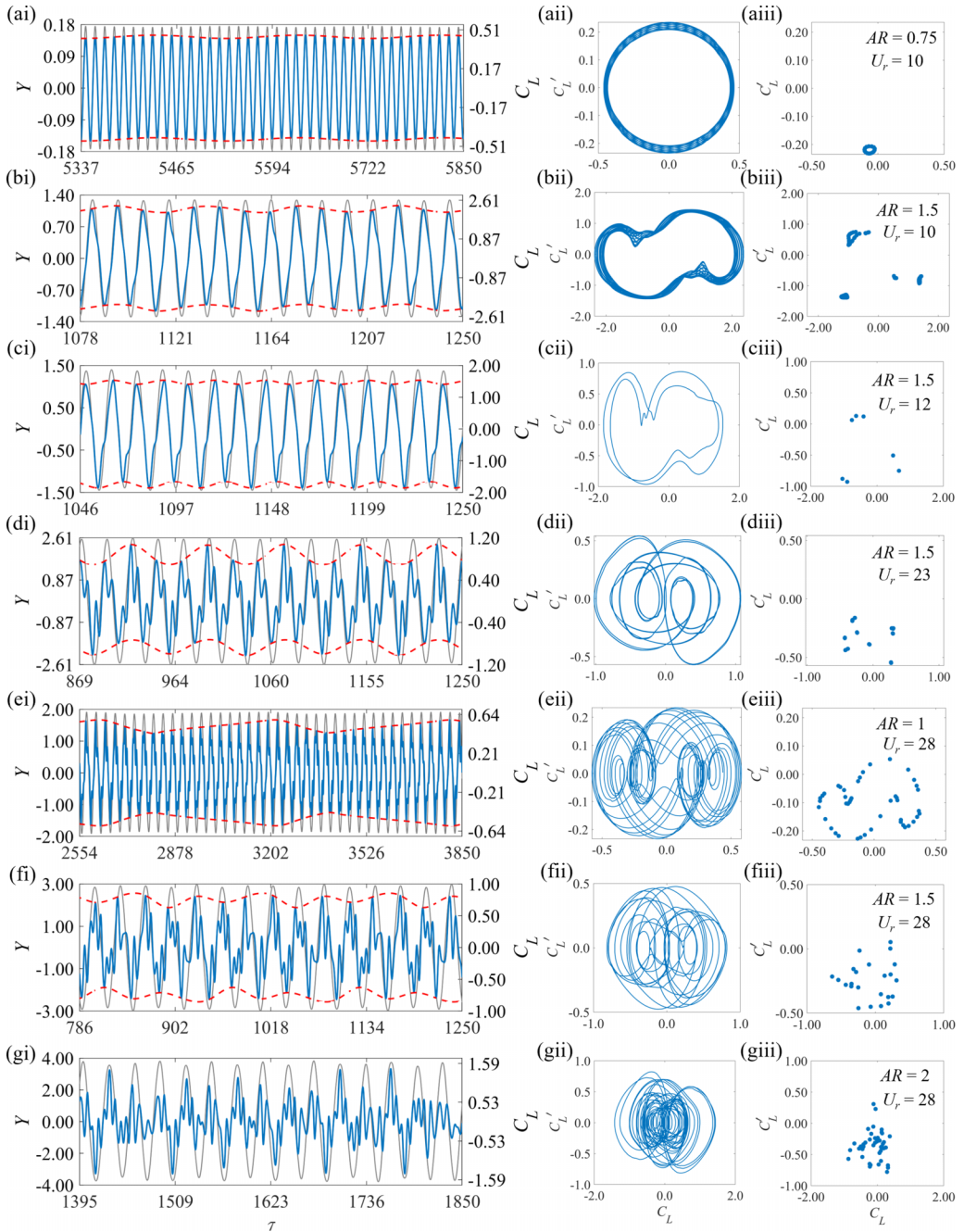


FIG. 14. Dynamical characteristics in the nonsynchronization branches of an elliptical cylinder-plate assembly with $L_{SP}/D = 0.75$ experiencing an unlimited flow-induced vibration (FIV). Each row of panels exhibits the results for the assembly for a given aspect ratio at a representative reduced velocity. The dynamical characteristics consist of (i) the time series $Y(t)$ (gray lines) and $C_L(t)$ (blue lines), (ii) phase portrait $C_L-C'_L$, and (iii) Poincaré section. The red dashed lines delineate the amplitude envelope of C_L .

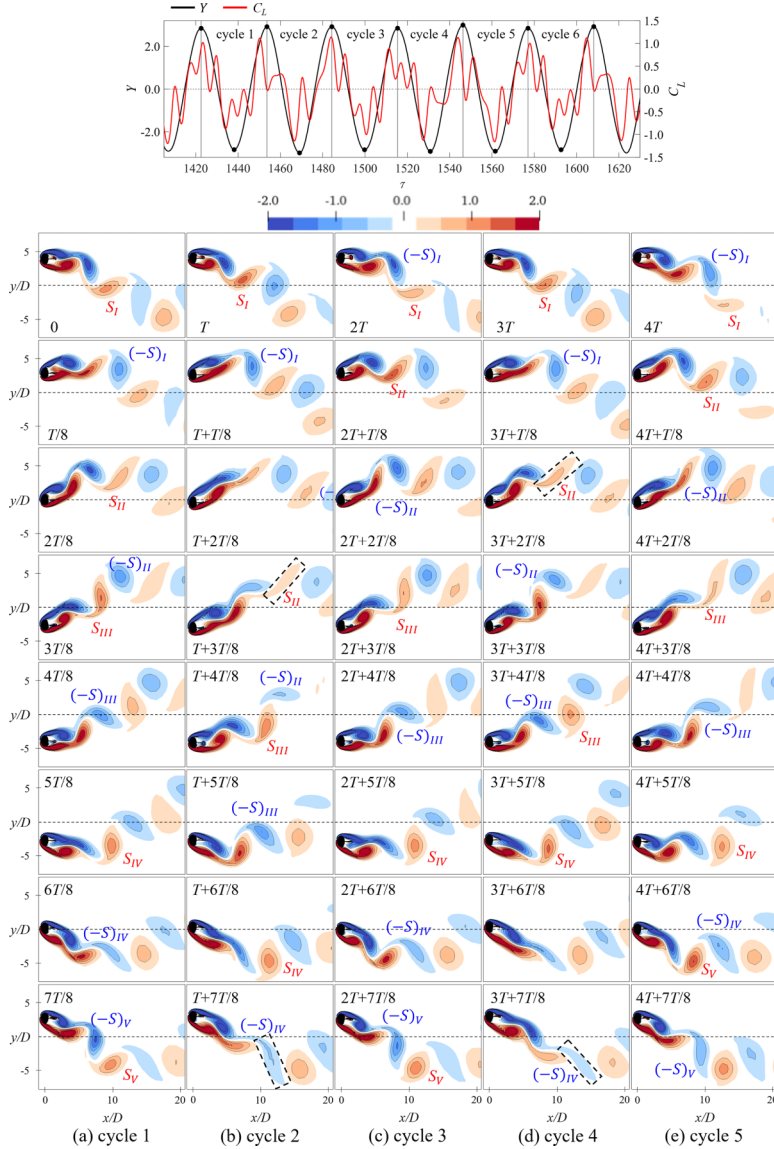


FIG. 15. The instantaneous vorticity field over five consecutive oscillation cycles for an elliptical cylinder-plate assembly with $L_{SP}/D = 0.75$ and aspect ratio $AR = 1.5$ at $U_r = 28$. This is an example of a period-5 oscillation.

galloping regime are observed for $AR = 1$. In addition, two special branches—the still branch (gray) and initial galloping branch (pink)—are identified based on their unique dynamical characteristics (viz., the steady-state dynamics of structure and flow for the former and the wake meandering for the latter). The corresponding PSD contours of f_Y/f_n and f_{C_L}/f_n exhibit a simple frequency structure. More details for this case are provided by Wu *et al.* [22]. When AR is increased from 1 to 1.5, the assembly still exhibits a clear-cut separation in the VIV and galloping responses. However, the branching behavior is significantly different, as is evident from an examination of Fig. 16(b). First, two even-multiple (i.e., 1:4 and 1:6) synchronization branches, with narrow U_r ranges, are present in the amplitude response at about $U_r = 14$ and 24, while the 1:3 synchronization branch is

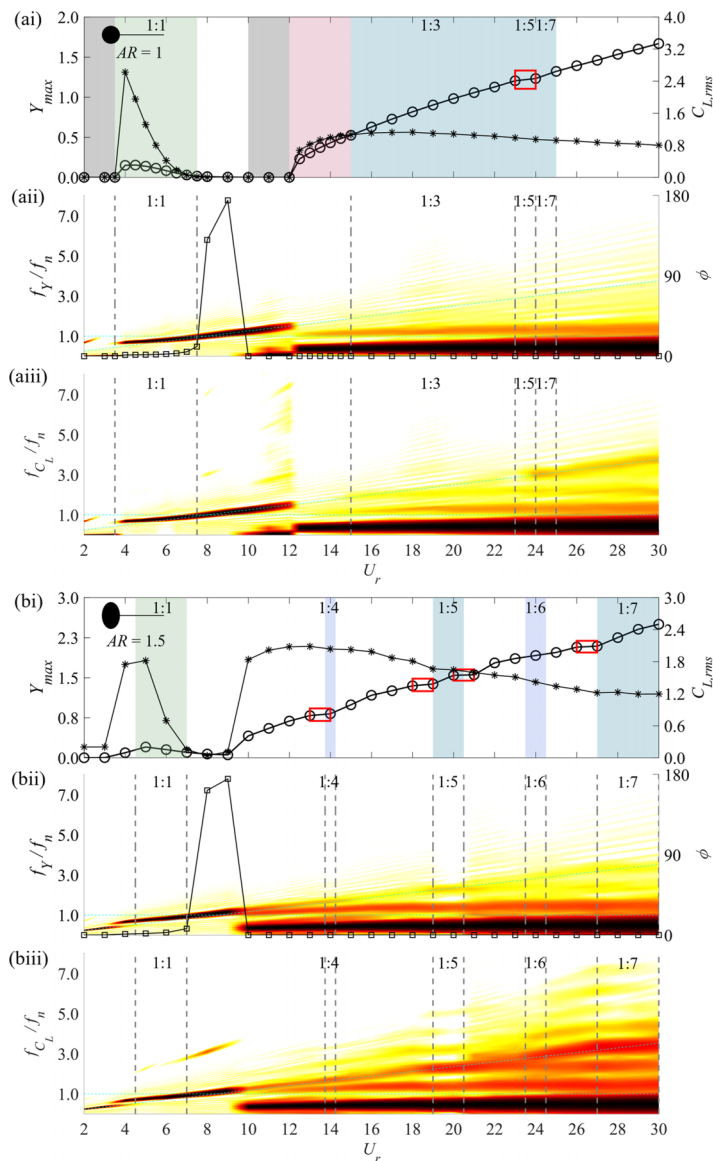


FIG. 16. The unlimited flow-induced vibration (FIV) response of an elliptical cylinder-plate assembly with $L_{SP}/D = 2.5$ for (a) and (b) aspect ratios $AR = 1$ and 1.5 . The dynamical characteristics are expressed in terms of the branching behavior and the power spectral density (PSD) of Y and C_L . Other notations used here are the same as those described in the captions of Figs. 4–6.

absent. Furthermore, the synchronization branches are separated from each other. Second, the still and initial galloping branches that are specific to a circular cylinder-plate assembly with a longer splitter plate are absent. The corresponding PSDs of f_Y/f_n and f_{C_L}/f_n are more complex than those for $AR = 1$, including stronger and higher-order harmonic components in the spectrum.

The vortex shedding in the synchronization branch is influenced by the AR . For $AR = 1$, Wu *et al.* [22] showed that the vortex-shedding patterns consist of a 2S mode in the lock-in, a $2 \times (P+S)$ mode in the 1:3 synchronization branch, no clear-cut identifiable mode in the 1:5 synchronization branch, and a $7 \times (2S)$ mode in the 1:7 synchronization branch. The vortices are elongated and

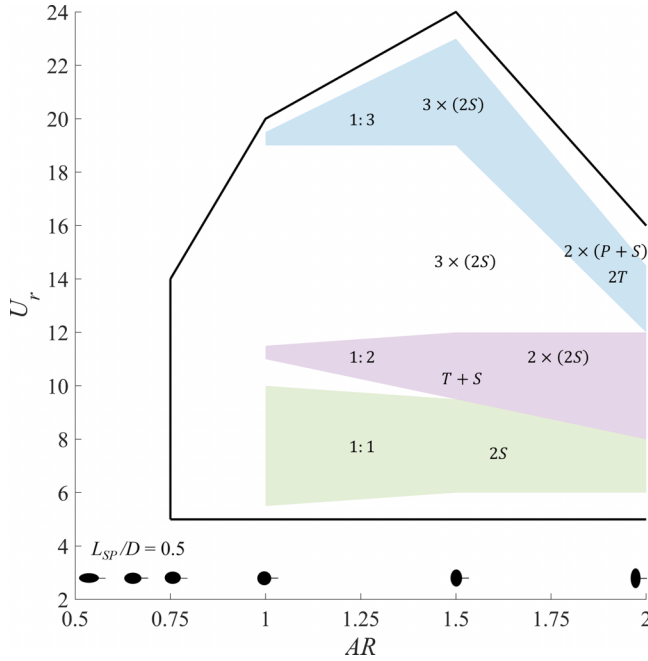


FIG. 17. The branching behavior and wake mode for an elliptical cylinder-plate assembly with $L_{SP}/D = 0.5$ in the [aspect ratio (AR), U_r] plane. The flow-induced vibration (FIV) response occurs over a limited reduced-velocity range.

connected. In marked contrast, for an elliptical cylinder-plate assembly with $AR = 1.5$, a much simpler vortex-shedding pattern is observed in the synchronization branches, namely, a $n \times (2S)$ wake mode with elliptically shaped vortices is associated with a $1:n$ synchronization branch.

It is concluded that a larger AR does not alter the nature of the dynamic response induced on an elliptical cylinder-plate assembly, which is primarily determined by the splitter-plate length (e.g., a self-limited FIV is provoked for an assembly with $L_{SP}/D = 0.5$ [23], an unlimited integrated VIV-galloping response appears for $L_{SP}/D = 0.75$, and a separated VIV and galloping response is provoked for $L_{SP}/D = 2.5$). However, larger AR affects the branching behavior of the amplitude response and the corresponding vortex-shedding pattern due to the significant increase in the complexity of the frequency content in the power spectrum of C_L . In some sense, a simultaneous increase in both AR and U_r can achieve the same effect with respect to the FIV response of an elliptical cylinder-plate assembly.

F. Maps of branching behavior and wake mode

Figures 17 and 18 compare the branching behavior and wake modes for an elliptical cylinder-plate assembly of various ARs experiencing vibration in a limited ($L_{SP}/D = 0.5$) and an unlimited ($L_{SP}/D = 0.75$) range of reduced velocity. The black solid lines delineate the effective range for the FIV response of the assembly. The region outside the black solid lines corresponds to the conditions in the (AR, U_r) plane where the assembly does not vibrate. The synchronization branches in the amplitude response are distinguished using different colors, and the nonsynchronization branches are shown in white. Except for the differences mentioned previously, more complex wake modes are observed in the synchronization branch for a limited FIV response, while more regular vortex-shedding patterns are observed in the synchronization branches for an unlimited FIV response.

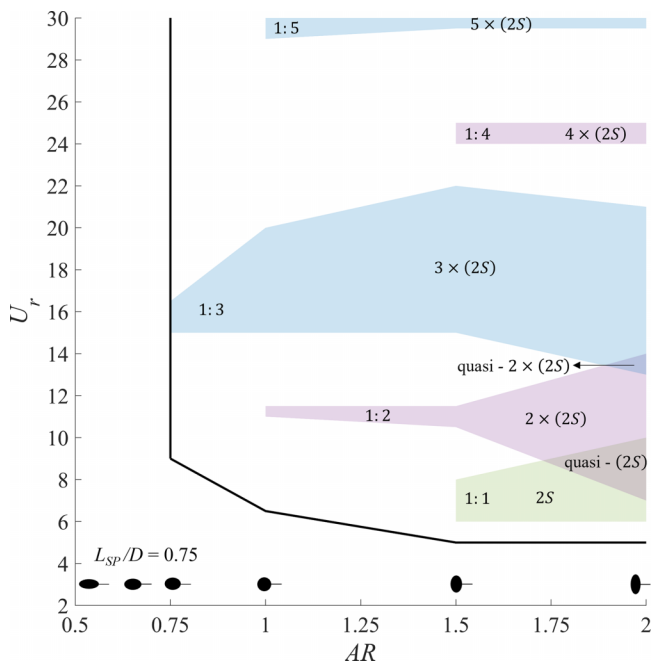


FIG. 18. The branching behavior and wake mode of an elliptical cylinder-plate assembly with $L_{SP}/D = 0.75$ in the [aspect ratio (AR), U_r] plane. The flow-induced vibration (FIV) response occurs over an unlimited reduced-velocity range.

IV. CONCLUSIONS

The effect of AR on the unlimited FIV response of an elliptical cylinder-plate assembly is investigated numerically at $Re = 100$, $m^* = 10$, and $\zeta = 0$.

The AR and the splitter-plate length stress on different aspects in influencing the FIV of the assembly. First, AR determines whether an oscillation can be triggered in the assembly—a critical value of $0.67 < AR_{cri} < 0.75$ is required for this to occur because the flow separation point on the windward surface of a horizontal ellipse is too far back to provoke an oscillatory motion [23]. Second, L_{SP} determines primarily the fundamental FIV mode to be limited or unlimited. Furthermore, a larger AR always provokes a stronger unlimited FIV through a reduction in the reduced-velocity associated with the onset of FIV and a concomitant increase in the vibration amplitude.

For an unlimited FIV response, increasing AR results in the generation of more synchronization branches in the amplitude response (e.g., 1:3 synchronization for $AR = 0.75$; 1:2, 1:3, and 1:5 synchronizations for $AR = 1$; and 1:1, 1:2, 1:3, 1:4, and 1:5 synchronizations for $AR = 1.5$ and 2). Accordingly, an unlimited FIV can transition from a pure galloping to an integrated VIV-galloping response. Transition regimes are present between the 1:1 and 1:2 and between the 1:2 and 1:3 synchronization branches in the amplitude response for the assembly with $AR = 2$.

A regular alternating vortex-shedding pattern is observed in the various synchronization branches—the pattern is associated with an $n \times (2S)$ wake mode for a 1: n synchronization branch. However, the vortex shapes are affected by the AR and the reduced velocity. For example, increasing AR results in the shedding of slender vortices at times corresponding to the amplitude maxima of the transverse displacement. Furthermore, increasing U_r results in a more vertical orientation (viz., oriented more strongly in the y direction) in the vortices. This leads to a subdivision of the 1:3 synchronization branches for an assembly with $AR = 1.5$ and 2. In addition, quasi-(2S) and

quasi- $2 \times (2S)$ modes are present in the transition regimes (viz., the regime between the 1:1 and 1:2 synchronizations and between the 1:2 and 1:3 synchronizations). The vortices shed in the transition regime consist of a combination of a primary elliptically shaped vortex and a secondary weaker tail-shaped vortex. The number of vortices shed in the transition regime is between those of the two synchronization branches that bracket it on either side. By contrast, the nonsynchronization branch is characterized by aperiodic oscillations [e.g., amplitude modulation of $C_L(t)$] and the period-doubling oscillation associated with the vortex-shedding pattern marking the transition from a lower-order to a higher-order synchronization branch.

ACKNOWLEDGMENTS

This paper was funded by the Natural Sciences and Engineering Research Council of Canada Discovery Grants Program Grant No. 50503-10234. It was made possible by the facilities of the Shared Hierarchical Academic Research Computing Network and Compute/Calcul Canada.

- [1] M. M. Bernitsas, K. Raghavan, Y. Ben-Simon, and E. Garcia, VIVACE (vortex induced vibration aquatic clean energy): A new concept in generation of clean and renewable energy from fluid flow, *J. Offshore Mech. Arct. Eng.* **130**, 041101 (2008).
- [2] Y. Wu, Z. Cheng, R. McConkey, F.-S. Lien, and E. Yee, Modelling of flow-induced vibration of bluff bodies: A comprehensive survey and future prospects, *Energies* **15**, 8719 (2022).
- [3] A. Nemes, J. Zhao, D. L. Jacono, and J. Sheridan, The interaction between flow-induced vibration mechanisms of a square cylinder with varying angles of attack, *J. Fluid Mech.* **710**, 102 (2012).
- [4] J. Zhao, J. S. Leontini, D. L. Jacono, and J. Sheridan, Fluid–structure interaction of a square cylinder at different angles of attack, *J. Fluid Mech.* **747**, 688 (2014).
- [5] S. Sen and S. Mittal, Free vibration of a square cylinder at low Reynolds numbers, *J. Fluids Struct.* **27**, 875 (2011).
- [6] J. Zhao, J. Leontini, D. L. Jacono, and J. Sheridan, The effect of mass ratio on the structural response of a freely vibrating square cylinder oriented at different angles of attack, *J. Fluids Struct.* **86**, 200 (2019).
- [7] B. Zhang, Z. Mao, B. Song, W. Ding, and W. Tian, Numerical investigation on effect of damping-ratio and mass-ratio on energy harnessing of a square cylinder in FIM, *Energy* **144**, 218 (2018).
- [8] B. Zhang, K.-H. Wang, B. Song, Z. Mao, and W. Tian, Numerical investigation on the effect of the cross-sectional aspect ratio of a rectangular cylinder in FIM on hydrokinetic energy conversion, *Energy* **165**, 949 (2018).
- [9] J. Zhao, K. Hourigan, and M. C. Thompson, An experimental investigation of flow-induced vibration of high-side-ratio rectangular cylinders, *J. Fluids Struct.* **91**, 102580 (2019).
- [10] H. Yu and M. Zhang, Effects of side ratio on energy harvesting from transverse galloping of a rectangular cylinder, *Energy* **226**, 120420 (2021).
- [11] Navrose, V. Yogeswaran, S. Sen, and S. Mittal, Free vibrations of an elliptic cylinder at low Reynolds numbers, *J. Fluids Struct.* **51**, 55 (2014).
- [12] J. Zhao, K. Hourigan, and M. C. Thompson, Dynamic response of elliptical cylinders undergoing transverse flow-induced vibration, *J. Fluids Struct.* **89**, 123 (2019).
- [13] H. Zhu, Y. Zhao, and T. Zhou, Numerical investigation of the vortex-induced vibration of an elliptic cylinder free-to-rotate about its center, *J. Fluids Struct.* **83**, 133 (2018).
- [14] H. Wang, Q. Zhai, and K. Chen, Vortex-induced vibrations of an elliptic cylinder with both transverse and rotational degrees of freedom, *J. Fluids Struct.* **84**, 36 (2019).
- [15] M. A. Shahzer, M. A. Khan, S. F. Anwer, S. A. Khan, M. S. Khan, A. Algethami, and M. Alsehli, A comprehensive investigation of vortex-induced vibrations and flow-induced rotation of an elliptic cylinder, *Phys. Fluids* **34**, 033605 (2022).

- [16] N. Shao, J. Lian, F. Liu, X. Yan, and P. Li, Experimental investigation of flow induced motion and energy conversion for triangular prism, [Energy](#) **194**, 116865 (2020).
- [17] H. Zhu, T. Tang, T. Zhou, M. Cai, O. Gaidai, and J. Wang, High performance energy harvesting from flow-induced vibrations in trapezoidal oscillators, [Energy](#) **236**, 121484 (2021).
- [18] B. Stappenbelt, Splitter-plate wake stabilisation and low aspect ratio cylinder flow-induced vibration mitigation, [Int. J. Offshore Polar Eng.](#) **20**, 1 (2010).
- [19] X. Sun, C. S. Suh, Z.-H. Ye, and B. Yu, Dynamics of a circular cylinder with an attached splitter plate in laminar flow: A transition from vortex-induced vibration to galloping, [Phys. Fluids](#) **32**, 027104 (2020).
- [20] M. Zhang, X. Wang, and O. Øiseth, Torsional vibration of a circular cylinder with an attached splitter plate in laminar flow, [Ocean Eng.](#) **236**, 109514 (2021).
- [21] M. Zhang, O. Øiseth, and F. Xu, Laminar flow-induced vibration of a three-degree-of-freedom circular cylinder with an attached splitter plate, [Phys. Fluids](#) **33**, 113605 (2021).
- [22] Y. Wu, F.-S. Lien, E. Yee, and G. Chen, Flow-induced vibration of cylinder-plate assembly at low Reynolds number: Branching behavior, [Phys. Fluids](#) **35**, 053612 (2023).
- [23] Y. Wu, F.-S. Lien, E. Yee, and G. Chen, Flow-induced vibration of an elliptic cylinder with a splitter-plate attachment at low-Reynolds number: Self-limited oscillations, [J. Fluids Struct.](#) **122**, 103985 (2023).
- [24] Y. Wu, F. S. Lien, E. Yee, and G. Chen, Numerical investigation of flow-induced vibration for cylinder-plate assembly at low Reynolds number, [Fluids](#) **8**, 118 (2023).
- [25] Y. Wu, F. S. Lien, and E. Yee, Nonlinear analysis of the flow-induced vibration of a circular cylinder with a splitter-plate attachment, [Commun. Nonlinear Sci. Numer. Simul.](#) **125**, 107403 (2023).